Numerical Analysis of RAP Elements under Dynamic Loading

by

Angela Saade

Thesis submitted to the faculty of the Virginia Polytechnic Institute and State University
in partial fulfillment of the requirements for the degree of

Master in Science
In
Civil Engineering

Alba Y. Colom
Russell A. Green
Bernardo A. Castellanos

November 28th, 2018
Blacksburg, VA

Keywords: Liquefaction, Numerical Model, Dynamic Loading, Rammed Aggregate Pier®, Christchurch

Copyright © 2018, Angela Saade
ALL RIGHTS RESERVED

Numerical Analysis of RAP Elements under Dynamic Loading

Angela Saade

ABSTRACT

The 2010-2011 Canterbury, New Zealand, Earthquake Sequence (CES) resulted in 185 fatalities and approximately $NZ40 billion in damage, much of which was due to liquefaction and related phenomena. As a result, an extensive soil improvement field testing program was initiated and Rammed Aggregate Piers™ (RAP) were shown to be a feasible method to mitigate the risk from liquefaction during future events. To better design and more fully assess the efficacy of reinforcement techniques against liquefaction, pre- and post-treatment in-situ test data are compiled, to include results from cone penetration tests (CPT), direct-push crosshole tests, and vibroseis (T-Rex) shaking tests. The data are used to evaluate the capabilities of numerical tools to predict the liquefaction response of unimproved and improved sites. A finite difference (FD) numerical model is developed in a FLAC platform and a coupled analysis using the Finn model with Byrne (1991) formulation is conducted. The FD model calibrated for top-down shakings similar to the vibroseis tests succeeded in qualitatively reproducing the general observed behavior without quantitatively matching the in-situ values for shear strains and excess pore pressure ratios. The introduction of the RAP elements to the FD model reduced the shear strain, but slightly overestimated that reduction. Considering more advanced constitutive models that better simulate the complexity of the soil behavior under dynamic loading would likely increase the accuracy of the predicted response.

Numerical Analysis of RAP Elements under Dynamic Loading

Angela Saade

GENERAL AUDIENCE ABSTRACT

During earthquakes, a significant loss of strength in soil can occur. This phenomenon, known as liquefaction, can have a devastating impact on the area affected. The 2010-2011 Canterbury, New Zealand, Earthquake Sequence (CES) resulted in 185 fatalities and approximately $NZ40 billion in damage, much of which was due to liquefaction and related phenomena. Consequently, the New Zealand Earthquake Commission implemented a field testing program in order to investigate the efficiency of ground improvement techniques in reducing soil liquefaction potential. One of the tested techniques was Rammed Aggregate Piers™ (RAP) and was shown to be a feasible method in mitigating the risk from liquefaction during future events. The focus of this study is to develop a numerical model capable of predicting the liquefaction response of unimproved and RAP-improved sites. Pre- and post-treatment test data are therefore compiled and used to calibrate the model. The numerical model calibrated for shakings similar to the on-site tests succeeded in qualitatively, but not quantitatively, reproducing the behavior observed in the field. The introduction of the RAP elements to the model revealed an improvement against liquefaction hazard; however, the improvement was overestimated compared to the field results. Considering more advanced numerical features that better simulate the complexity of the soil behavior under dynamic loading would likely increase the accuracy of the predicted response.

Dedication

To a very beautiful soul who was always a great example in faith, love and perseverance. Thank you for keeping an eye on me. I love you and I miss you grandma Angèle.

Acknowledgements

This research was funded by Geopier Foundation Company. Dr. Russell Green provided guidance and feedback throughout the work. Dr. Jorge Macedo Escudlero assisted with aspects related to the FLAC simulations. Additionally, Ms. Sneha Upadhyaya assisted with some of the New Zealand data selection process. This support and assistance are gratefully acknowledged. I extend a special mention to Dr. Alba Yerro and Dr. Russell Green for their continuous support and encouragement throughout the course of my graduate studies. However, any opinions, findings and conclusions or recommendations expressed in this material are those of the authors and do not necessarily reflect the views of Geopier Foundation Company.

Table of Contents

Chapter 1: Introduction

1.1 Problem Statement

The main objective of this study is to use pre- and post-treatment in-situ data from the Christchurch, New Zealand, field testing program to calibrate a finite difference (FD) numerical model and assess its capability in predicting the liquefaction response of unimproved and improved sites. Among the different ground improvement techniques, Rammed Aggregate Pier® (RAP) elements are selected for this study. Earthquake induced soil liquefaction can cause major disasters and economic losses and mitigating its risk through ground improvement technique is a major focus of geotechnical earthquake engineers. This study presents the process involved in developing a numerical model capable of validating the effectiveness of such ground improvement techniques.

1.2 Organization

This thesis is organized into three chapters and 6 appendices (A-F). The second chapter is a manuscript anticipated to be submitted as conference paper. The third chapter provides a summary of the work conducted, the key findings and recommendations for future work. The back matter of the thesis contains 6 appendices which provide supplementary details on the evaluation of the liquefaction potential at the studied site, the estimation of material properties from CPT and DPCH testing, the calibration of the material properties for unreinforced FD model, the output results for vertical stress, pore pressure, and volumetric strain distributions obtained for the unreinforced FD model, the V_s profile for the deconvolution analysis, and the sign conventions and system of units in FLAC v.8.

1.3 Attribution

The manuscript in Chapter 2 entitled: “Numerical Analysis of RAP Elements under Dynamic Loading,” authored by A. Saade et al. will be submitted for consideration as a conference paper. The following provides a list of the contributing co-authors and their primary roles on this paper.

Alba Yerro, Ph.D., Department of Civil and Environmental Engineering at Virginia Tech, Blacksburg, Virginia, USA.

- Research Advisor to the lead author and provided significant guidance, reviews and support during all phases of this research. Dr. Yerro is also credited for her major contributions in developing numerical methods in geotechnical engineering.

Russell A. Green, Ph.D., Department of Civil and Environmental Engineering at Virginia Tech, Blacksburg, Virginia, USA

- Research co-Advisor to the lead author and provided guidance and his expertise on the subject throughout the research. Dr. Green is also credited for his major contributions in developing procedures for assessing liquefaction potential, which are used in this study.

Jorge Macedo, Ph.D., Department of Civil and Environmental Engineering at Georgia Tech, Atlanta, Georgia, USA

- Provided guidance in the design of the numerical model.

Kord Wissmann, Ph.D., Geopier Foundation Company, North Carolina, USA

- Sponsor of the project

Chapter 2: Numerical Analysis of RAP Elements under Dynamic Loading

2.1 Abstract

The 2010-2011 Canterbury, New Zealand, Earthquake Sequence (CES) resulted in 185 fatalities and approximately $NZ40 billion in damage, much of which was due to liquefaction and related phenomena. As a result, an extensive soil improvement field testing program was initiated and Rammed Aggregate Piers™ (RAP) were shown to be a feasible method to mitigate the risk from liquefaction during future events. To better design and more fully assess the efficacy of reinforcement techniques against liquefaction, pre- and post-treatment in-situ test data are compiled, to include results from cone penetration tests (CPT), direct-push crosshole tests, and vibroseis (T-Rex) shaking tests. The data are used to evaluate the capabilities of numerical tools to predict the liquefaction response of unimproved and improved sites. A finite difference (FD) numerical model is developed in a FLAC platform and a coupled analysis using the Finn model with Byrne (1991) formulation is conducted. The FD model calibrated for top-down shakings similar to the vibroseis tests succeeded in qualitatively reproducing the general observed behavior without quantitatively matching the in-situ values for shear strains and excess pore pressure ratios. The introduction of the RAP elements to the FD model reduced the shear strain, but slightly overestimated that reduction. Considering more advanced constitutive models that better simulate the complexity of the soil behavior under dynamic loading would likely increase the accuracy of the predicted response.

2.2 Introduction

Earthquake induced soil liquefaction can have devastating effects on infrastructure and the economy of the impacted region. Disasters and economic losses directly associated with liquefaction have been observed in almost every major earthquake (Eseller-Bayat et al. 2009; Woeste et al. 2016). According to Kramer (1996), liquefaction is a complex phenomenon that mainly occurs in loose, saturated sandy soils. Under repeated stresses, the tendency of the soil skeleton to contract results in the overburden stresses transferring from the soil skeleton to the pore fluid, increasing excess pore pressures and reducing

effective stress (Woeste et al. 2016). Consequently, liquefaction can result in a significant loss in soil strength, large cyclic and shear deformations, and flow failures (Youd et al. 2001).

Efforts to better understand the phenomenon and its effects, as well as to develop techniques to mitigate its risk, are continuously being investigated both in research and in practice. Ground improvement techniques are being validated to ensure their effectiveness in mitigating the risk due to liquefaction. Comparison of pre- and post-improvement in-situ testing is one form of validation which ensures that the construction technique achieves the required level improvement (Woeste et al. 2016). Observing the performance of improved ground during and after earthquakes is another form to validate common ground improvement techniques (Mitchell et al. 1995; Mitchell and Martin 2000; Hausler and Sitar 2001; Wotherspoon et al. 2014; Woeste et al. 2016). However, this approach requires continuous collection and analysis of case history data and can be very time-intensive. An alternative method of validation is to conduct full scale field testing which can provide detailed site-specific information but can also be expensive and unwieldy. However, advanced numerical modelling can provide insights into the liquefaction response of improved ground that cannot be obtained by more global validation approaches. Towards this end, model calibration is key to obtaining reliable results from the numerical analyses (Ziotopoulou and Boulanger 2015).

The aim of the work presented herein is to compile a database of pre- and post-treatment in-situ test data and use the data to calibrate a finite difference numerical model that can be used to predict liquefaction response under a wide range of loading conditions. For this purpose, data from the Christchurch, New Zealand, field testing program that was performed following the 2010-2011 Canterbury Earthquake Sequence (CES) is used. Among the different tested ground improvement techniques, the focus herein is on the Rammed Aggregate Pier® (RAP) elements.

2.3 Christchurch Soil Improvement Field Testing Program

The Christchurch, New Zealand, testing program that was performed following the 2010-2011 CES offers a substantial amount of data that can be used to study the effectiveness of ground improvement techniques in mitigating the liquefaction hazard. The CES induced widespread ground deformation and lateral spreading resulting in 185 fatalities and 51,000 damaged residential properties, among which 15,000 were damaged beyond economical repair (van Ballegooy et al. 2015; Wissmann et al. 2015; Roberts 2017).The analysis of the aftermath of the CES highlighted the vulnerability of Christchurch's built environment. However, regional scale geotechnical investigation showed that less structural damage was recorded in areas where liquefiable soils were overlain by roughly 3-m of stiff non-liquefying crust (van Ballegooy et al. 2015, Wentz et al. 2015). This observation is in good agreement with an earlier statement from Ishihara (1985): "the conditions for avoiding liquefaction-induced damage would be to have a mantle of unliquefiable soils thicker than about 3.0 m when the thickness of the underlying liquefiable sand layer is larger than 3.0 m." Taking this into account and considering the urgent need to mitigate the risk from liquefaction during future events, the New Zealand Earthquake Commission (EQC) initiated a testing program where the effectiveness of shallow ground improvement methods for creating a non-liquefiable crust were assessed. The trial program was conducted in three locations in Christchurch along the Avon River (Sites 3, 4 and 6), where severe liquefaction damage was recorded during the CES (Wissmann et al. 2015). The actual location of the program sites can be found in Roberts 2017.

The trial program consisted of constructing full-scale test panels of natural and improved soils and conducting various in-situ testing. The ground improvement techniques evaluated included Rammed Aggregate Pier™ (RAP) reinforcement, Rapid Impact Compaction (RIC), Driven Timber Poles (DTP), Low Mobility Grout (LMG), Resin Injection (RES), Gravel Rafts (GR), Soil-Cement Rafts (SCR), and Horizontal Soil-Cement Mixed (HSM) beams (van Ballegooy et al. 2015; Wissmann et al. 2015; Roberts 2017). The in-situ testing phase included excavation trenching, cone penetration testing (CPT), direct-push crosshole shear wave velocity testing (DPCH), and vibroseis T-Rex shaking (van Ballegooy et al.

2015; Wissmann et al. 2015; Roberts 2017). Figure 1 provides the locations of the test panels performed at Site 6. Pre- and post-improvement CPT soundings were performed in order to study the change in measured tip resistance (q_c). The DPCH testing provides measurement of small strain shear and compression wave velocities (V_s and V_p, respectively).

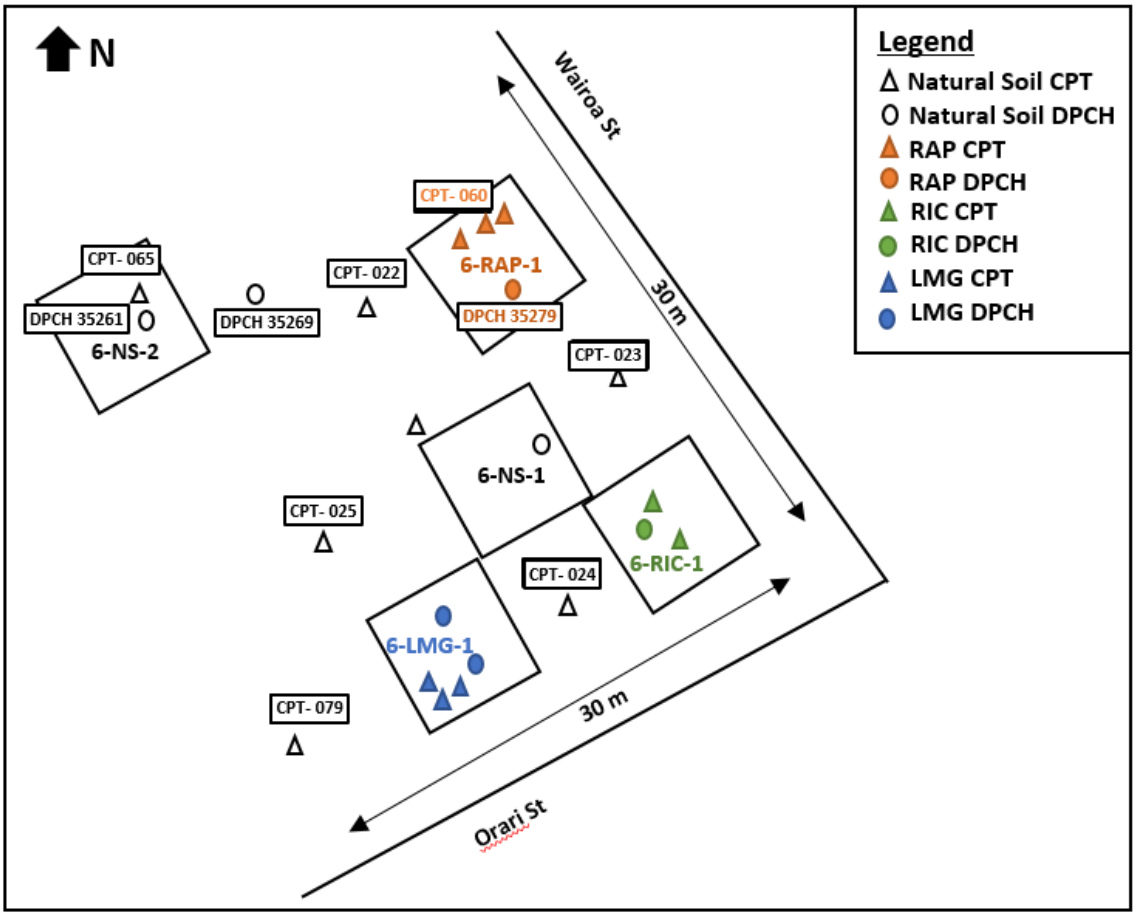

Figure 1: Test panels performed at Site 6 (After Roberts 2017)

The soil profiles observed after trenching graded from sandy silt and silty sand to clean sand at deeper locations. Table 1 provides the information obtained from the excavation trench conducted in the natural soil test Panel 6-NS-2 at Site 6.

Table 1: Information from excavation trench at the 6-NS-2 Test Panel. (After Roberts 2017)

Layer	Depth Range	F.C (%)	USCS	Description
1	0 – 0.6 m	-	SP-SM	Fine to medium SAND some organics; dark brown; loose; moist; rootlets (FILL)
2	0.6 – 1.0 m	96	ML	SILT with trace organics; grey and brownish orange; homogenous; stiff; non-plastic; dilatent
3	1.0 – 1.25 m	74	ML	Sandy SILT; grey; homogenous; stiff; non-plastics; dilatent
4	1.25 -1.9 m	3-25	SM	Silty fine SAND; grey; homogenous; loose; wet
5	1.9 – 3.3 m	3	SW	Fine to medium SAND with trace silt

Additionally, the T-Rex shaking test gives good indication of the treated sites liquefaction response by relating the cyclic shear strain and the accumulation of excess pore pressures. The shaker applies dynamic oscillating shear loads at the ground surface having a specified frequency and cycle number. The dynamic loading from the T-Rex equipment was horizontally applied at a frequency of 10 Hz for 100 cycles over a 2.3-m square baseplate. The load was applied in stages going from 3,000 lbs to 30,000 lbs, corresponding to cyclic stresses varying from 2.5 kPa to 25 kPa. Moreover, the T-Rex truck imparts a vertical load equal to 245 kN resulting in a static pressure of 46 kPa beneath the baseplate**.** Figure 2 illustrates the T-Rex shaking test. Pore pressure and velocity transducers installed directly beneath the shaker record the soil response for the specific load magnitude (Figure 3). Generated pore pressures and velocity histories are directly measured. Displacements are obtained from the velocity histories and cyclic shear strain is calculated by evaluating relative displacements between adjacent transducers. The T-Rex testing is capable of assessing liquefaction triggering at shallow depths, down to 4 m below the surface, and therefore provides important data to examine the efficacy of the ground improvement techniques in developing non-liquefying crust (van Ballegooy et al. 2015).

2.4 RAP Reinforcement Technique

The results obtained for the different ground improvement panels compared to those from the unimproved soils indicated that all the techniques succeeded in stiffening the upper 4 m of the profiles (Roberts 2017). However, the current work focuses on the improvement against liquefaction recorded at the RAP panels. Nine areas were improved using RAP at the three different sites in Christchurch (Sites 3, 4, and 6). Hydraulic pressure and vertical vibratory hammer energy were used to displace and densify the soil, while crushed aggregates were fed and compacted in the cavities, creating 600-mm diameter stiff piers that were 4 m in length. The elements were constructed in a triangular pattern (plan view) with the center-to-center spacing varying from 1.5 to 3.0 m, and the RAP-reinforced areas were tested using the previously described in-situ tests (Figure 2).

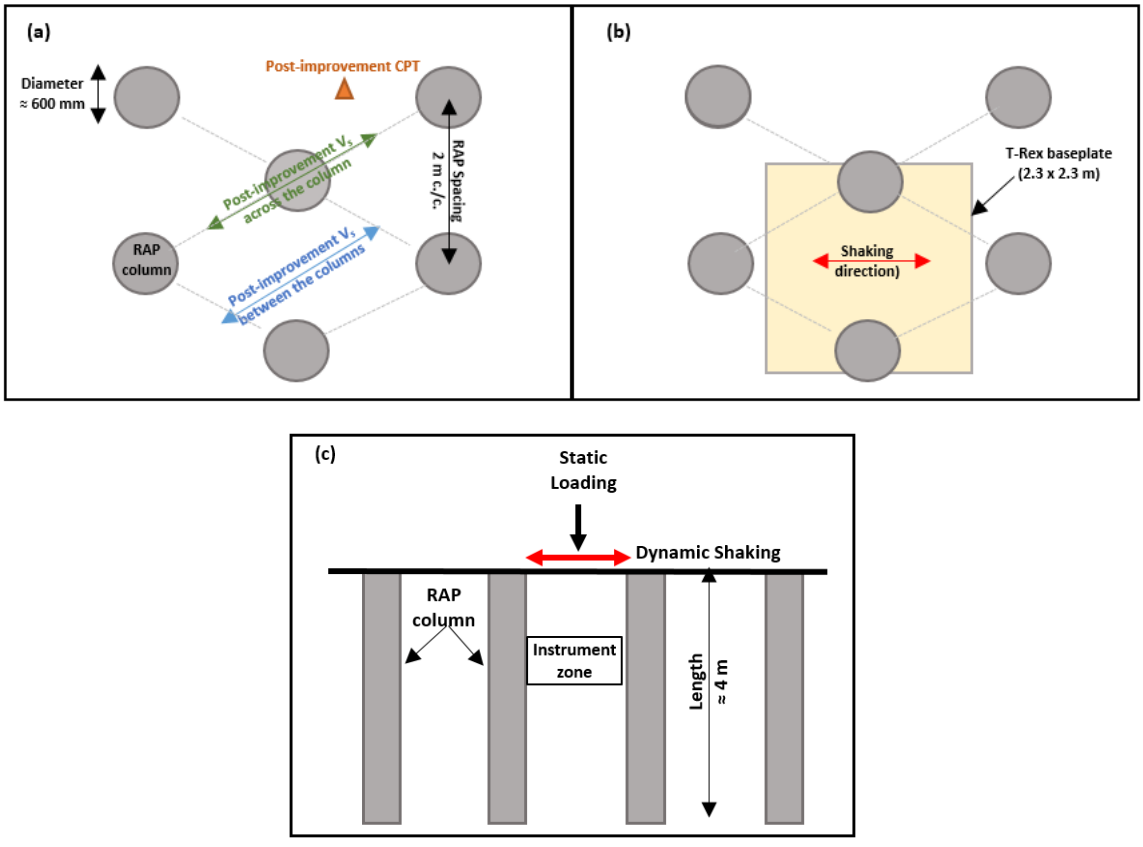

Figure 2: (a) CPT and DPCH testing relative to the RAP columns; (b) Schematic top view of T-Rex baseplate relative to the RAP columns; and (c) Schematic cross section of the T-Rex shaking in the RAP test panel (After van Ballegooy et al. 2015).

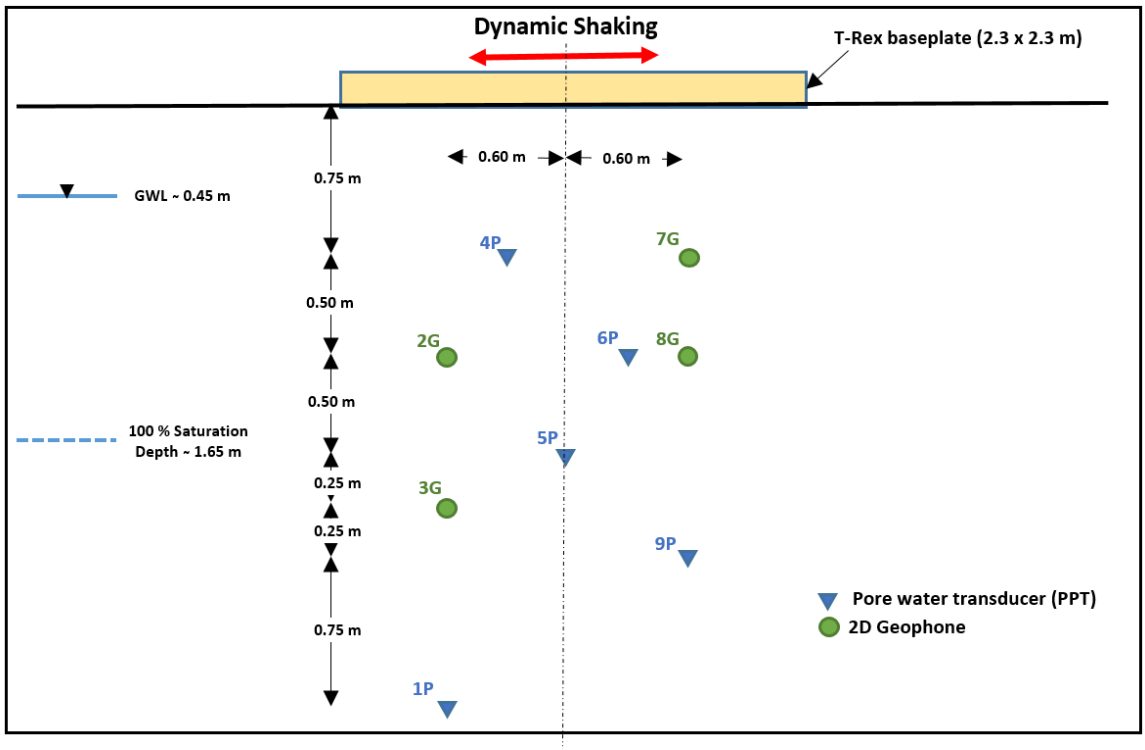

Figure 3: Cross section of the sensors' locations beneath the T-Rex baseplate for natural soil and RAP test panels at Site 6. (After Stokoe et al. 2013)

The CPT data show that, in general, the RAP elements are effective in increasing q_c and, consequently, in increasing the ability of the soil to resist liquefaction. However, for layers of higher fines content corresponding to a soil behavior type index (Ic) greater than 1.8, minimum change in q_c was recorded, suggesting less improvement. Unlike the CPT results, clear improvement in small strain shear modulus (G_{max}) occurred both in clean and silty layers, hence reduction in liquefaction potential, even for finer soils, can be expected (van Ballegooy et al. 2015). The results of the direct-push crosshole testing indicate that the greatest increases in stiffness in the areas improved using RAP occurred across the elements. In fact, the presence of the stiff piers induces a major increase in the composite V_s values and consequently results in 40 to 130% increase in the composite G_{max} values (van Ballegooy et al. 2015). The assessment of the cyclic shear strain profiles obtained from the T-Rex shaking also indicates that the greatest reduction in cyclic shear strains occurred in the RAP reinforced soil. An average decrease of 37% with respect to unimproved soil was recorded, suggesting an improvement in the composite stiffness by a

factor of 3 to 5 (van Ballegooy et al 2015; Wissmann et al. 2015; Roberts 2017). As the composite stiffness increases, the potential for development of excess pore pressure declines, and the potential liquefaction hazard under cyclic loading diminishes.

The conclusions obtained from the CPT, direct-push crosshole testing, and T-Rex testing are all in good agreement and highlight the improvement created by the inclusion of stiff gravel piers, making the RAP technique generally effective to reduce liquefaction susceptibility in both clean and silty soils.

2.5 Evaluation of the Liquefaction Potential: Site 6

The Green et al. (2018a) CPT-based simplified liquefaction triggering procedure was used to evaluate the liquefaction response of the test sites. Due to space limitations, focus herein is only on Site 6, for which data from six CPT sounding are available for unimproved conditions (Figure 1). Two earthquakes from the 2010-2011 CES responsible for much of the widespread liquefaction-related damage in Christchurch are considered herein: the 4 September 2010, M_w7.1 Darfield earthquake and the 22 February 2011, M_w6.2 Christchurch earthquake. The geometric mean of the horizontal peak ground accelerations (a_{max}) at the test sites during these two events were estimated using the Bradley (2013) and Bradley (2017) ground motion prediction models and the estimated values are provided in Appendix A. Given that the a_{max} values predicted by the two models differ, both values were used in the analyses. The water table depth at the time of the earthquakes was obtained from van Ballegooy et al. (2014), whereas the level of water at the time of testing was estimated from the CPT sounding data (Appendix A). The factor of safety (FS) against liquefaction is calculated as:

$$FS = \frac{CRR_{7.5}}{CSR^*}$$

where CSR* is the Cyclic Stress Ratio normalized for a shaking duration of a M_w7.5 event, level ground conditions, and an effective overburden stress of 100 kPa; and $CRR_{7.5}$ is the Cyclic Resistance Ratio normalized for the same conditions as CSR*, where both CSR* and $CRR_{7.5}$ were determined using the procedures detailed in Green et al. (2018a). Likewise, Ic was also determined following the procedures detailed in Green et al. (2018a),

where soils having an Ic less than 2.6 were assumed to be susceptible to liquefaction and soils having an Ic greater than 2.6 were considered "too clayey to liquefy" (Robertson and Wride 1998). For non-liquefiable soils an arbitrary high value of FS equal to five was adopted in order to visually detect these layers on the graphs. Similarly, soils above the water table were assumed to be non-liquefiable and were also assigned an FS value of five. Both the Liquefaction Potential Index (LPI) (Iwasaki et al. 1978) and "Ishihara inspired LPI" (LPI_{ish}) (Maurer et al. 2015) frameworks were used to relate the computed FS with depth to the severity of surficial liquefaction manifestations. Inherently, the LPI and LPI_{ish} frameworks assume that each liquefying soil layer contributes to the severity of liquefaction at the ground surface, with the LPI_{ish} framework better accounting for the influence of the non-liquefied crust on the severity of surficial liquefaction manifestations (Maurer et al. 2015; Green et al. 2018b). The shallower and/or thicker the liquefied layers in a profile, the greater their potential contribution to severity of surficial liquefaction manifestations, relative to deeper soil layers. Using Standard Penetration Test (SPT) data from 45 liquefaction sites in Japan, Iwasaki et al. (1978) found that 80% of the sites had LPI > 5, while 50% had LPI > 15. Based on this data, it was proposed that severe liquefaction damage should be expected for sites where LPI > 15 but should not be expected for sites where LPI < 5. This criterion for severity of surficial liquefaction manifestation, defined by two threshold values of LPI, is commonly used in practice, and is also adopted herein as the criterion for LPI_{ish} (Maurer et al. 2015).

For each CPT sounding, Ic, corrected q_c (q_{c1Ncs}), FS, LPI, and LPI_{ish} are plotted against elevation. Representative results for CPT 022 for the 22 February 2011, M_w6.2 Christchurch earthquake are provided in Figure 4 and Figure 5. The a_{max} value obtained from Bradley (2013) is estimated to be equal to 0.523 g, whereas that obtained from Bradley (2017) is equal to 0.431 g. The representative results in Figure 4 and Figure 5 correspond to the higher value of a_{max} equal to 0.523 g. According to Roberts (2017), the actual depth to 100% saturation at Site 6 varies between 0.9 m to 1.2 m below the water table. Therefore, the zone corresponding to less than 100% saturation were hatched on the graphs but no further considerations for unsaturated conditions were made at this time.

Water tables corresponding to the level of water at the time of the earthquake and at the time of CPT testing are both shown on the graphs.

Most of the Ic values are below 2.6 indicating that the soil is susceptible to liquefaction, except for thin layers of clayey soil detected at few locations. Furthermore, the FS graph suggests a high liquefaction hazard, especially for the upper layers of the profile. The LPI and LPI_{ish} values of 27.6 and to 25.7, respectively, are greatly above the threshold of 15 for severe surficial liquefaction manifestations. The results for the other CPT soundings across Site 6 are consistent with those for CPT 022 (Figure 4 and Figure 5) and suggest the same conclusions (Appendix A). The results from the simplified liquefaction procedure and the LPI and LPI_{ish} indices are clearly in accord with post-earthquake observations.

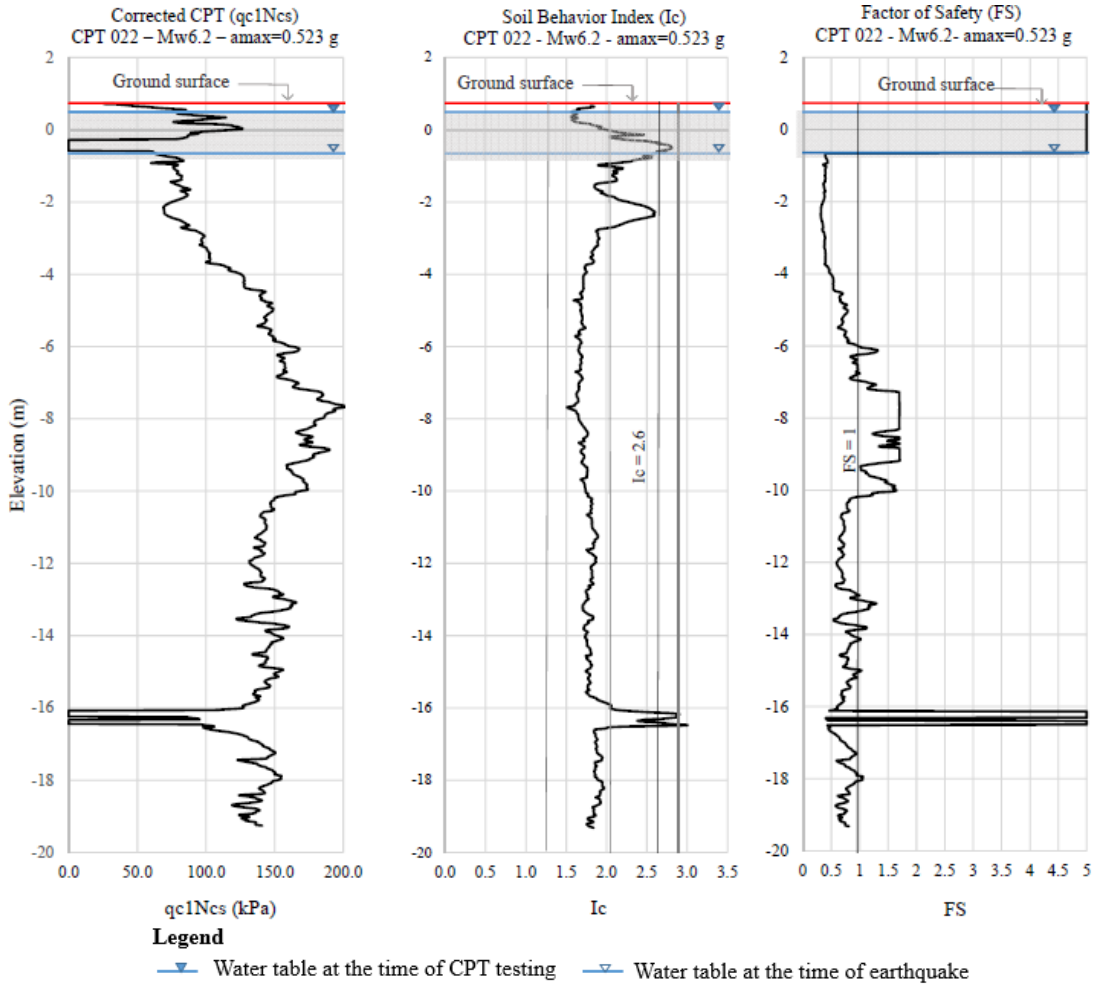

Figure 4: q_{c1Ncs}, Ic, and FS for CPT 022: Mw6.2 & a_{max} = 0.523 g

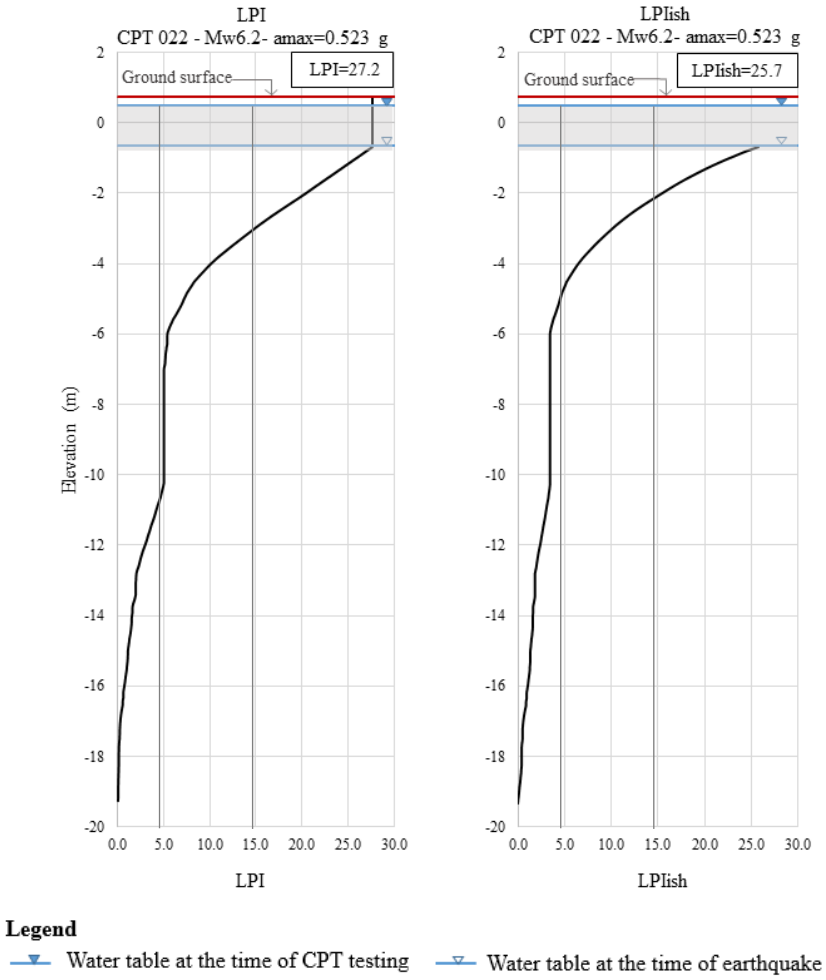

Figure 5: LPI, and LPI_{ish} for CPT 022: M_w6.2 & a_{max} = 0.523 g

2.6 Estimation of Material Properties from CPT and DPCH Testing: Site 6

2.6.1 Estimation of geotechnical material properties from CPT

CPT tests were conducted at Site 6, Christchurch (Figure 1) and q_c and sleeve friction (f_s) from the CPT soundings are downloaded from the New Zealand Geotechnical Database (https://www.nzgd.org.nz). The CPT can provide a guide to the normalized soil behavior type (SBT_n) and the mechanical characteristics of the soil. Semi-empirical correlations provided in the 6th Edition of the *Guide to Cone Penetration Testing for Geotechnical Engineering* (Robertson and Cabal 2015) are used to estimate the geotechnical soil parameters at the natural soil test panel 6-NS-2 from CPT 022 and CPT 065, and at the

improved panel 6-RAP-1 from CPT 060 (Figure 1).The SBT_n is estimated from the soil behavior index Ic using Table 2. Appendix B provides the correlations used to calculate Ic and the equivalent clean sand cone penetration resistance ($(Q_{tn})_{cs}$) following Robertson and Cabal (2015).

For unimproved conditions, the Ic profiles showing the SBT_n zones and $(Q_{tn})_{cs}$ profiles are plotted for CPT 022 and CPT 065 (Figure 6 and Figure 7 respectively). Changes in Ic and $(Q_{tn})_{cs}$ profiles suggest changes in the soil behavior type and allow the determination of the different existing soil layers. Eight layers are identified from the 20-meter CPT 022 which are reduced to six layers for the 5-meter CPT 065 as shown is Figure 6 and Figure 7. The layers identified for the upper 3.3 m of unimproved soils are consistent with the soil profile obtained from the test pit log.

Table 2: Normalized CPT soil Behavior Type (SBT_n). (After Robertson 2010)

Zone	Soil Behavior Type	Ic
1	Sensitive, fine grained	N/A
2	Organic soils - clay	> 3.6
3	Clays - silty clay to clay	2.95-3.6
4	Silt mixtures - clayey silt to silty clay	2.60-2.95
5	Sand mixtures - silty sand to sandy silt	2.05-2.6
6	Sands - clean sand to silty sand	1.31-2.05
7	Gravelly sand to dense sand	<1.31
8	Very stiff sand to clayey sand*	N/A
9	Very stiff, fine grained*	N/A
* Heavily overconsolidated or cemented		

For each CPT data point, Standard Penetration Test values (N_{60}), corrected N_{60} value for overburden stresses ($N_{1,60}$), unit weight, relative density, friction angle, and hydraulic conductivity values are calculated using the CPT correlations provided in Appendix B. An average value for each parameter is calculated over the thickness of the layer and is assigned to the entire layer. Table 3 summarizes the unimproved soil properties estimated from CPT 022 and CPT 065 soundings and Table 4 provides the post-improvement soil properties estimated from CPT 060 sounding.

The values obtained for the unit weights are compatible with the values provided by Roberts (2017) where the moist unit weight is estimated to be equal to 17 kN/m^3 and the total unit weight is estimated to be equal to 19.5 kN/m^3.

The relative density values predicted by the simplified Kulhawy and Mayne (1990) and the Jamiolkowski et al. (2001) correlations are in good agreement, whereas the Baldi et al. (1986) correlation tends to estimate higher values of the relative density for some layers and lower values for other layers. In fact, for soils with fines, the relative density obtained from empirical correlations using CPT may be difficult to ascertain (Roberts 2017).

The values of the friction angle estimated using the Robertson and Campanella (1983) and Kulhawy and Mayne (1990) correlations are fairly comparable and lay within typical representative ranges of values for the given soil types. However, Robertson and Campanella (1983) correlation seems to estimate higher values of the friction angle for some layers.

The deeper soil layers for post-improvement conditions show increase in properties. However, a drop in N_{60}, relative density, and friction angle is recorded in the upper 1 m of the improved soil (Table 4) compared to the unimproved condition (Table 3). This decrease in soil properties conforms to the observation made in Roberts (2017) suggesting a softer and looser soil for the top 1 m of RAP reinforced profile compared to natural profiles.

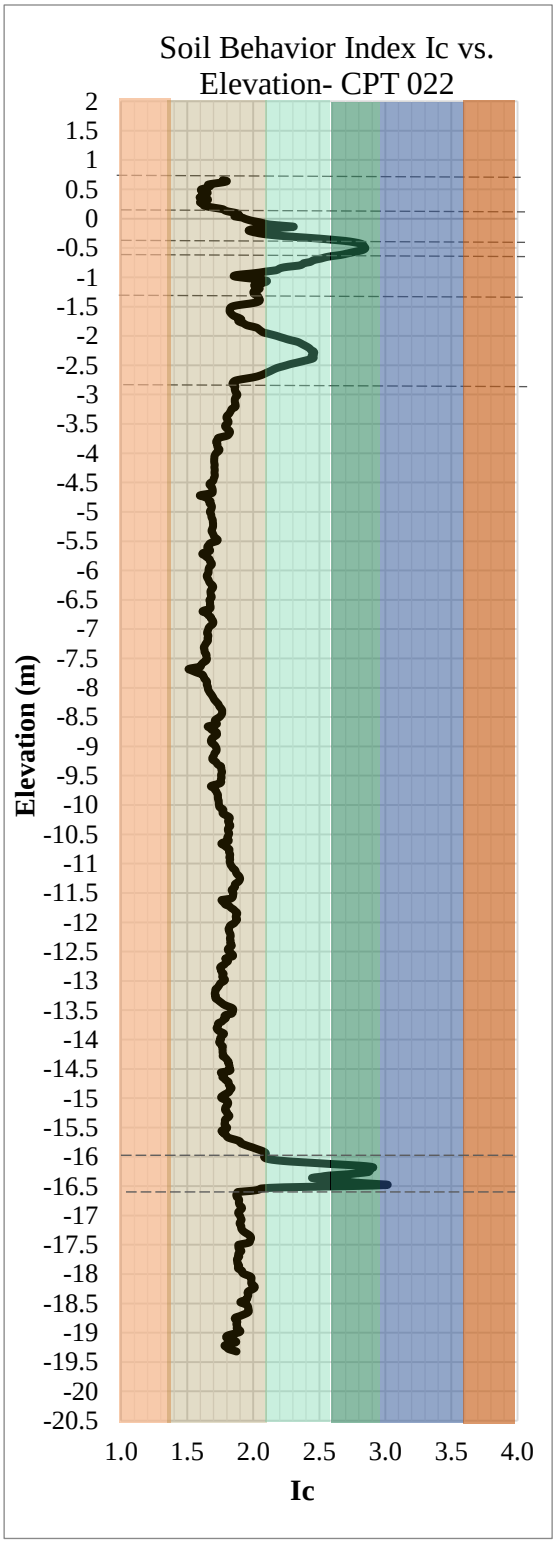

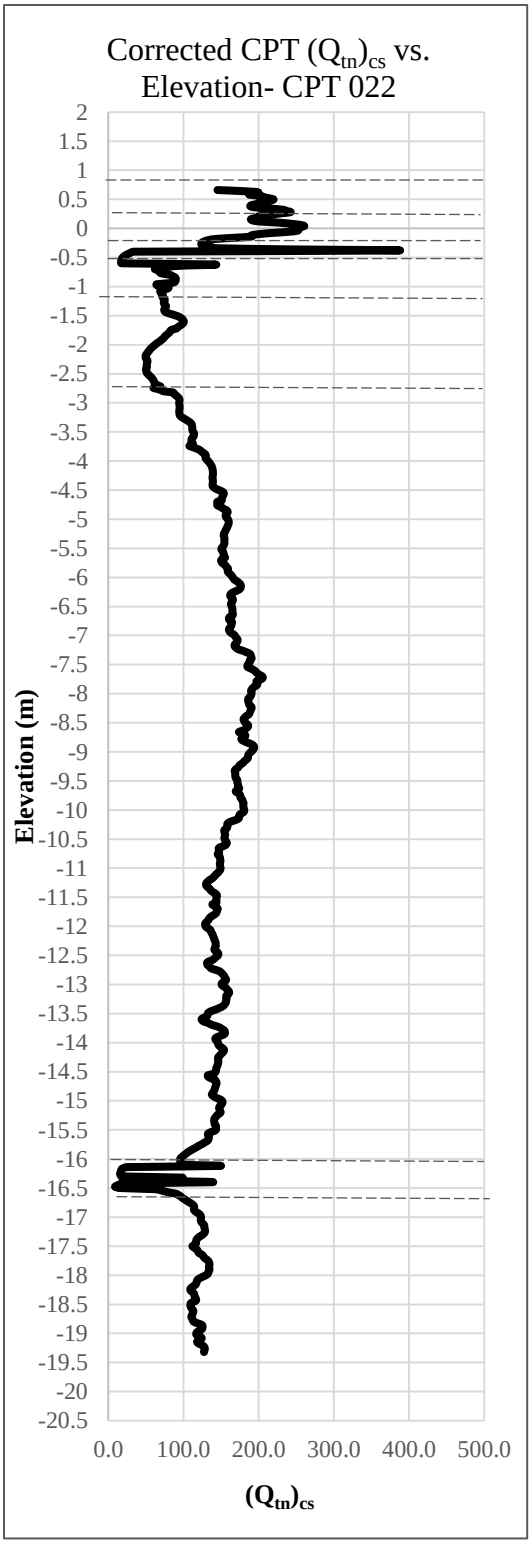

Figure 6: Ic and $(Q_{tn})_{cs}$ profiles for CPT022

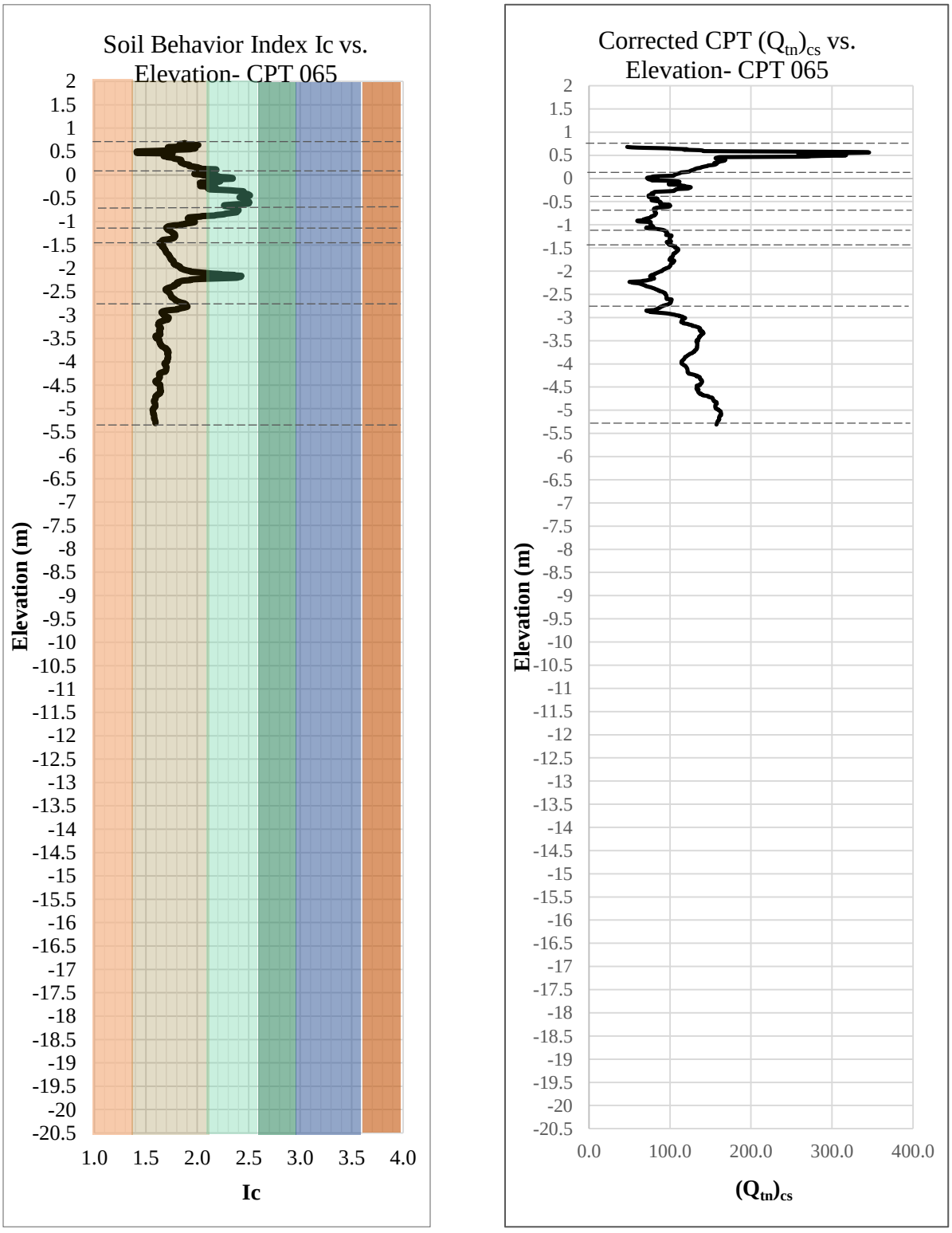

Figure 7: Ic and $(Q_{tn})_{cs}$ profiles for CPT065

Table 3: Estimated unimproved soil properties obtained from CPT 022 and CPT 065 soundings

CPT 022											
Depth (m)	**N_{60} (blows/30 cm)**	**$N_{1,60}$ (blows/30 cm)**	**Unit weight (kN/m^3)**	**Relative Density (%)**			**Friction Angle (deg)**		**Hydraulic conductivity (m/s)**	**Soil Behavior Zone**	**Soil Behavior Type**
				Jamiolkowski et al. (2001)	Simplified Kulhawy and Mayne (1990)	Baldi et al. (1986)	Robertson and Campanella (1983)	Kulhawy and Mayne (1990)			
0 - 0.6	10	20	18	78	75	107	51	43	8E-05	6	Sands - Clean sand to silty sand
0.6 -1	10	18	18	62	66	82	47	41	1E-05	5	Sand Mixtures - Silty sand to sandy silt
1 - 1.25	3	5	17	14	34	7	37	35	4E-07	4	Silt Mixtures - Clayey silt to silty clay
1.25 - 1.65	2	4	15	8	28	0	35	33	5E-07	5	Sand Mixtures - Silty sand to sandy silt
1.65 - 1.9	6	9	16	39	41	46	41	37	4E-06		
1.9 - 3.3	6	9	16	31	36	35	38	36	7E-06	5	Sand Mixtures - Silty sand to sandy silt
3.3-16.75	33	32	19	67	63	91	43	41	5E-05	6	Sands - Clean sand to silty sand
16.75-17.25	18	14	19	28	27	29	32	33	5E-07	4	Silt Mixtures - Clayey silt to silty clay
17.25-20	39	31	20	61	53	81	39	39	1E-05	6	Sands - Clean sand to silty sand

CPT065											
Depth (m)	**N_{60} (blows/30 cm)**	**$N_{1,60}$ (blows/30 cm)**	**Unit weight (kN/m^3)**	**Relative density (%)**			**Friction Angle (deg)**		**Hydraulic conductivity (m/s)**	**Soil Behavior Zone**	**Soil Behavior Type**
				Jamiolkowski et al. (2001)	Simplified Kulhawy and Mayne (1990)	Baldi et al. (1986)	Robertson and Campanella (1983)	Kulhawy and Mayne (1990)			
0 - 0.6	7	14	17	68	70	92	46	40	9E-05	6	Sands - Clean sand to silty sand
0.6 -1	5	9	17	38	43	46	42	38	4E-06	5	Sand Mixtures - Silty sand to sandy silt
1 - 1.25	3	5	16	18	31	14	37	34	7E-07	5	Sand Mixtures - Silty sand to sandy silt
1.25 - 1.65	5	7	17	25	34	25	38	35	2E-06	5 -6	Sands - Sand Mixtures :Silty sand to sandy silt
1.65 - 1.9	10	13	17	49	46	62	42	38	3E-05		
1.9 - 3.3	13	16	17	52	49	67	42	39	4E-05	5-6	Sands - Sand Mixtures: Silty sand to sandy silt
3.3-6	22	25	18	65	60	87	43	41	9E-05	6	Sands - Clean sand to silty sand

Table 4: Estimated post-improvement soil properties obtained from CPT 060 sounding

CPT 060											
Depth (m)	**N_{60} (blows/30 cm)**	**$N_{1,60}$ (blows/30 cm)**	**Unit weight (kN/m^3)**	**Relative Density (%)**			**Friction Angle (deg)**		**Hydraulic conductivity (m/s)**	**Soil Behavior Zone**	**Soil Behavior Type**
				Jamiolkowski et al. (2001)	Simplified Kulhawy and Mayne (1990)	Baldi et al. (1986)	Robertson and Campanella (1983)	Kulhawy and Mayne (1990)			
0 - 0.6	5	10	17	57	60	74	47	40	6.E-05	5 and 6	Sands - Sand mixtures
0.6 -1	5	5	16	9	30	0	36	34	3.E-07	4 and 5	Sand mixtures - Silt mixtures
1 - 1.25	10	15	18	60	57	79	45	40	5.E-05	6	Sands - Clean sand to silty sand
1.25 - 1.65	15	25	18	72	68	98	46	42	1.E-04		
1.65 - 1.9	20	30	19	77	73	105	47	43	2.E-04		
1.9 - 3.3	30	35	19	79	77	109	47	43	2.E-04		
3.3-6	30	35	19	76	73	104	45	43	2.E-04		

2.6.2 Estimation of elastic material properties from DPCH

The elastic moduli of the unimproved soil (natural soil) at the test panel 6-NS-2 are estimated using the DPCH soundings 35261 and 35269 which are in the proximity to the test panel. Soil properties after the reinforcement are estimated from DPCH 35279 at the test panel 6-RAP-1 (Figure 1). The correlations used to estimate the shear modulus (G), Young's modulus (E) and Poisson's ratio (ν) from the V_s values are provided in Appendix B. Table 5 and Table 6 provide the unimproved elastic properties estimated from DPCH 35261 and 35269, respectively, whereas Table 7 provides the post-improvement soil properties obtained from DPCH 35279 across the RAP columns as shown in Figure 2a. The post-improvement results show a clear increase in the shear modulus with a median change of 130 % with respect to unimproved conditions.

Table 5: Estimated unimproved elastic properties from DPCH 35621

DPCH 35261					
Depth (m)	**Average p-wave velocity (m/s)**	**Average s-wave velocity (m/s)**	**Shear Modulus (MPa)**	**Poisson's Ratio**	**Young's Modulus (MPa)**
0 - 0.6	381	102	18	0.46	53
0.6 -1	730	102	18	0.49	54
1 - 1.25	1154	98	17	0.5	50
1.25 - 1.65	1366	105	19	0.5	57
1.65 - 1.9	1614	119	28	0.5	85
1.9 - 5.0	1678	153	47	0.5	139

Table 6: Estimated unimproved elastic properties from DPCH 35629

DPCH 35269					
Depth (m)	**Average p-wave velocity (m/s)**	**Average s-wave velocity (m/s)**	**Shear Modulus (MPa)**	**Poisson's Ratio**	**Young's Modulus (MPa)**
0 - 0.6	524	126	28	0.47	81
0.6 -1	597	139	34	0.47	99
1 - 1.25	1078	140	34	0.49	102
1.25 - 1.65	1547	140	34	0.5	101
1.65 - 1.9	1595	141	40	0.5	119
1.9 - 5.0	1606	157	49	0.5	146

Table 7: Estimated post-improvement elastic properties from DPCH 35279

DPCH 35279					
Depth (m)	Average p-wave velocity (m/s)	Average s-wave velocity (m/s)	Shear Modulus (MPa)	Poisson's ratio	Young's Modulus (MPa)
0 - 0.6	424	138	39	0.44	113
0.6 - 1	531	132	36	0.47	104
1 - 1.25	622	142	41	0.47	121
1.25 - 1.65	1274	192	75	0.49	223
1.65 - 1.9	1583	218	112	0.49	333
1.9 - 5.0	1713	256	153	0.49	457

2.7 Numerical Modeling

2.7.1 Numerical model technique and computer code

Among the various numerical modelling techniques, the explicit finite difference (FD) method is a powerful tool that is capable of modeling coupled stress-flow problems under static and dynamic loading conditions and can predict dynamic structure-soil interaction due to its ability to simulate large deformations and dynamic behavior of soils. Among the different FD computer codes, Fast Lagrangian Analysis of Continua (FLAC) is selected for the analysis. FLAC has important features for liquefaction problems such as stable large strain formulation and built-in Finn model that allows computation of excess pore pressure induced by dynamic shaking (Soroush and Koohi 2004). Considering adequate material constitutive models cyclic response of saturated soil and liquefaction processes can be modeled.

Nevertheless, to obtain reliable results and accurate predictions of liquefaction triggering when performing numerical simulations of realistic seismic shakings, experimental and/or field data are required to calibrate and validate the FD model.

2.7.2 Data available for calibration

The Christchurch database discussed above from full-scale tests in natural and reinforced soil is essential to calibrate and validate the FD numerical model. The initial estimation of

the soil properties is obtained from the CPT and DPCH testing as described in section 2.6 and the output from the FD model is calibrated against the measured data provided by the T-Rex shaking test.

Data from five pore water pressure transducers (4P, 6P, 5P, 9P and 1P) embedded at the test panels (Figure 3) are considered for calibration. All points were located below the water table which was encountered at an average depth of 0.45 m from the ground surface (Figure 3). The pore pressure histories collected from the transducers were used to compute excess pore pressure ratio (r_u) which is equal to the excess pore water pressure divided by the initial vertical effective stresses. According to Roberts (2017), the initial vertical effective stress in the soil was evaluated using a total unit weight of 17 kN/m^3 for soils above water table and 19.5 kN/m^3 for soils below water table. An additional 46 kPa vertical stress was considered to account for the vertical load imparted by the T-Rex baseplate (van Ballegooy et al. 2015). The initial hydrostatic water pressure was determined from measurements taken by the pressure transducers immediately before each stage of shake testing (Roberts 2017). The variations of r_u versus time at the transducers for the highest and lowest T-Rex loadings (25 kPa and 2.5 kPa respectively) are provided in Figure 8. Note that r_u oscillates and at some locations tends to increase during the loading. The magnitude of the oscillations generally decreases with depth and lower external loads. When the loading is released, r_u smoothly decreases to zero, which indicates the dissipation of excess pore water pressure.

The shear strain profiles were calculated by evaluating relative displacements derived from the velocity histories. The maximum shear strain for each loading was then adjusted to a nominal level of applied shear stress at the ground surface (van Ballegooy et al. 2015). Figure 9 provides the stiffness profiles for two levels of shear stress 15 and 5 kPa at the unimproved and RAP improved test panels at Site 6. Shear strain decreases logarithmically with depth in unimproved ground (6-NS-1 and 6-NS-2). For the RAP reinforced test panel (6-RAP-1), the curvature in the upper part of the profile suggests a stiffer soil at the surface which does not conform to the observation made from the CPT results discussed in section 2.6.1.

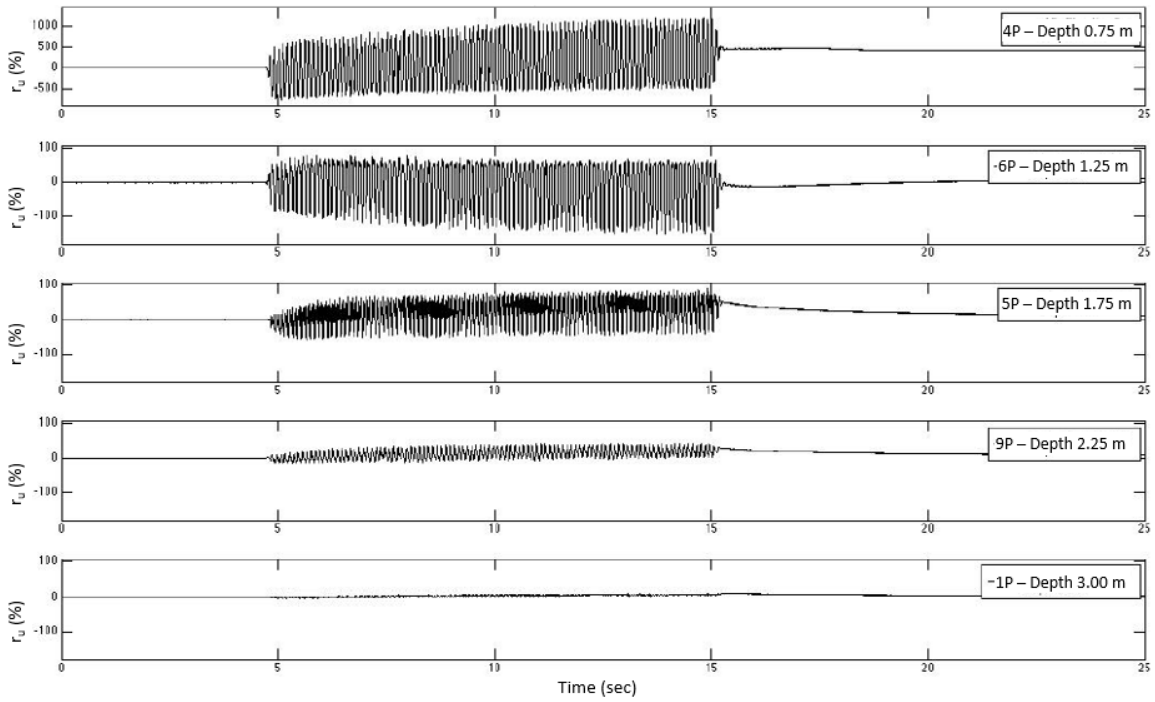

(a)

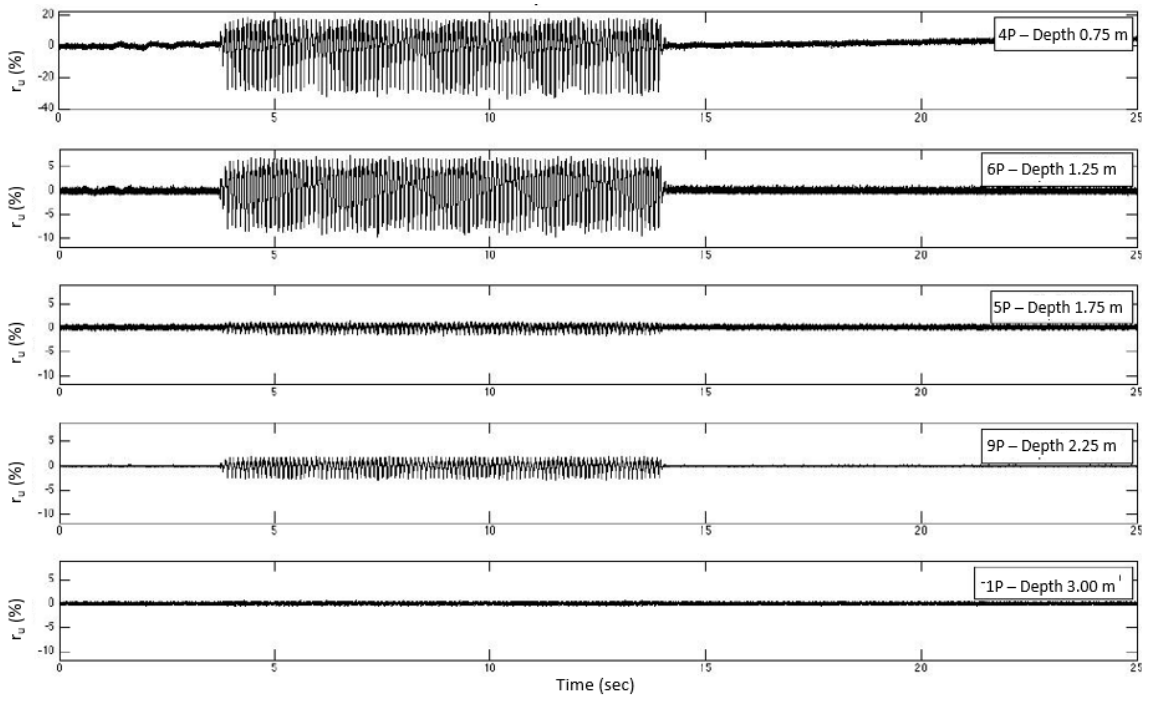

(b)

Figure 8: r_u vs. time for the unimproved soil panel at Site 6 (a) 25 kPa, (b) 2.5 kPa, applied for 100 cycles at 10 Hz. (After Stokoe et al. 2013)

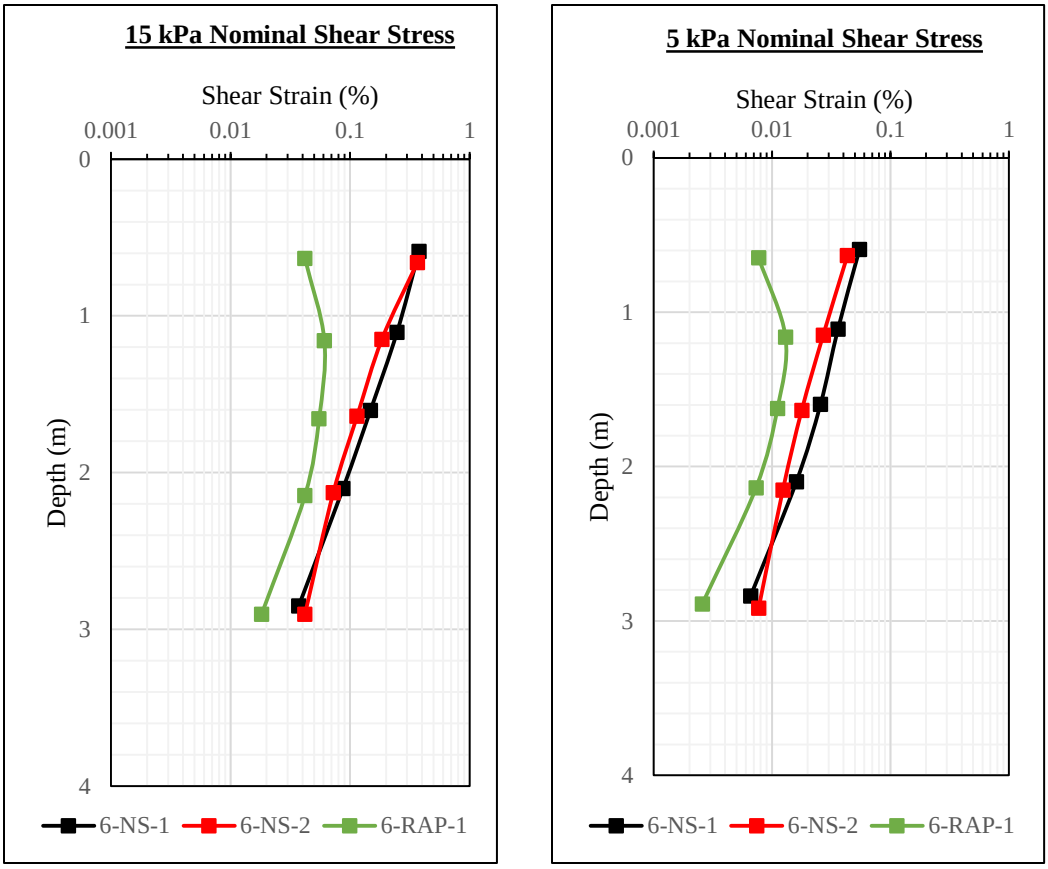

(a) **(b)**

Figure 9: Stiffness profiles for unimproved and improved test panels at Site 6 for a shear stress of (a) 15 kPa; and (b) 5kPa. (After Roberts 2017)

2.7.3 Modeling phases

At the first stage of the analysis, a top-down shaking similar to the in-situ T-REX loading is applied. The simulation allows the FD model to be calibrated to the in-situ conditions. Unreinforced conditions are first considered then RAP elements are introduced to the model to assess the response of reinforced soils under the dynamic top-down shaking. The second stage of the analysis consists on applying a bottom-up shaking at the base of the unreinforced and reinforced models in a way to simulate a real earthquake shaking.

2.8 Unreinforced FD Model: Top-Down Shaking

A FLAC model for unimproved soil conditions at Site 6 is first developed and a loading similar to the T-REX in-situ loading is applied.

2.8.1 Model geometry

A 2D plane strain analysis is considered. The model height is equal to 10 m and the width is equal to 50 m. Seven horizontal soil layers consistent with field measurements are defined as given in Figure 10.

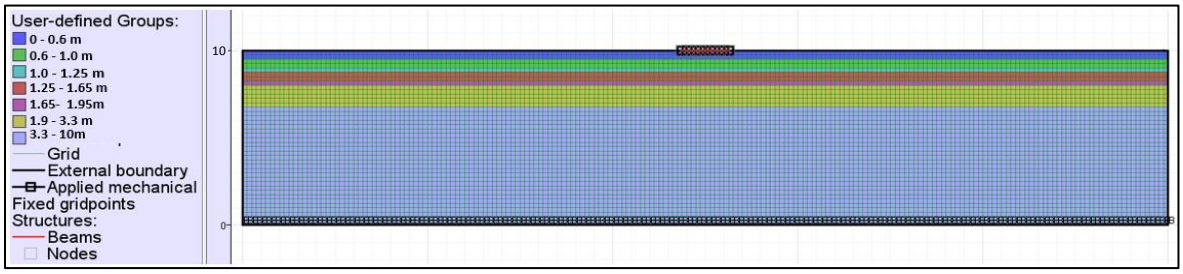

Figure 10: Geometry of the unreinforced FD model

The FLAC model is divided into 0.25-m square elements. The mesh size is defined in a way to ensure precise calculations, provide reasonable runtimes, and minimize numerical distortion of the propagating wave. The numerical accuracy of wave transmission is dependent on the frequency content and the speed of the input wave. The fundamental frequency (*f*) associated with the natural mode of oscillation of a system is calculated as:

$$f = \frac{C}{\lambda}$$

where C is the velocity of propagation associated with the mode of oscillation, and λ is the longest wavelength associated with the mode of oscillation. According to Kuhlemeyer and Lysmer (1973), the spatial element size (Δl), must be smaller than one-tenth of the wavelength associated with the highest frequency component ($\Delta l = \lambda / 10$). Therefore, the frequency can be written as follows:

$$f = \frac{C}{10\Delta l}$$

Based on the DPCH test, the lowest recorded shear wave velocity in the unimproved soils is equal to 98 m/s (Table 5). When the largest zone size in the FLAC model is selected to be 0.25 m, the maximum frequency that can be accurately modeled is approximately equal to 40 Hz, greater than the frequency content of the input wave, ensuring an accurate wave transmission.

2.8.2 Coupled analysis

The groundwater flow configuration is selected in order to have full access to the fluid-mechanical features in FLAC. The use of this configuration allows the performance of a fully coupled hydro-mechanical analysis that allows for the deformation of the solid skeleton, and the generation and dissipation of excess pore water pressures.

2.8.3 Mechanical boundary conditions

In dynamic problems, outward propagating waves can reflect at the fix boundaries and go back into the model without allowing the necessary energy dissipation. To reduce these artificial numerical oscillations, numerical boundaries should be defined reasonably far from the studied area. In addition, at the bottom of the model, the "quiet boundary" scheme proposed by Lysmer and Kuhlemeyer (1969) and available in FLAC is applied. It involves independent dashpots attached to the boundary in the normal and shear directions providing viscous normal and shear tractions. Taking advantage of the symmetry of the problem, lateral boundaries are considered "attached" boundaries; hence identical conditions are ensured in both sides, minimizing the artificial reflections.

2.8.4 Hydraulic boundary conditions

The water table is defined at 0.5 m depth from the surface, compatible with the in-situ conditions provided in Figure 3. The saturation level is fixed at that same location throughout the calculation. Above that saturation level, pore pressures are fixed equal to zero and no generation of pore pressures is allowed. Below the water table, soil layers are considered fully saturated. Impermeable hydraulic conditions are imposed at the lateral and bottom boundaries preventing any flow in or out of the model.

2.8.5 Mechanical constitutive model

In the field, during cyclic loading, grains rearrange and irrecoverable volume contraction of loose soil matrix can occur. As a result, pore pressure builds up and liquefaction can be triggered. The accumulation of fluid pressure is therefore a secondary effect to the changes in pore volume caused by the mechanical behavior of the solid matrix.

Because the standard Mohr-Coulomb failure criterion cannot account for shear and volumetric strain coupling, the Finn model is coupled to the Mohr-Coulomb criterion to account for the plastic volumetric strains. The original Finn model proposed by Martin et al. (1975) provides an empirical correlation between the cyclic shear-strain amplitude and the increment of volume decrease as:

$$\Delta\varepsilon_{vd} = C_1^{c}.(\gamma - C_2^{c}.\varepsilon_{vd}) + \frac{C_3^{c}.(\varepsilon_{vd})^2}{\gamma + C_4^{c}.\varepsilon_{vd}}$$

where $\Delta\varepsilon_{vd}$ is the increment of volume decrease, ε_{vd} is the accumulated unrecoverable volume strain, γ is the cyclic shear strain or "engineering shear strain", and C_1^{c}, C_2^{c}, C_3^{c} and C_4^{c} are constants.

A simpler alternative formula is proposed by Byrne (1991) as:

$$\frac{\Delta\varepsilon_{vd}}{\gamma} = C_1^{c} \exp(-C_2^{c}(\frac{\varepsilon_{vd}}{\gamma}))$$

where C_1^{c} and C_2^{c} can be derived from the normalized standard penetration test values $N_{1,60}$ as follows:

$$C_1^{c} = 8.7(N_{1,60})^{-1.25} \text{ and } C_2^{C} = \frac{0.4}{C_1^{c}}$$

The Byrne (1991) is widely used in the field and is considered to be a significantly improved and simplified version of Martin et al. (1975) equation. The Finn model with Byrne formulation is adopted for the analysis.

2.8.6 Loading process

The stresses are initialized subjected to gravity. Afterwards, an external loading equivalent to the in-situ loading (applied by the T-Rex equipment) is considered on the ground surface centered in the model. A vertical stress of 46 kPa equivalent to a vertical load of 245 kN imparted by the T-Rex truck baseplate is applied. Then, a sinusoidal horizontal stress with a frequency of 10-Hz is imposed for a period of 10 seconds while maintaining the vertical stresses constant. Both the horizontal and vertical stresses are applied over a 2.5-m plate, which is simulated by a set of structural beams slaved in the vertical direction.

2.8.7 Control points

Five control points located at the position of the original transducers 4P, 6P, 5P, 9P and 1P (Figure 3) are defined as per Figure C. 1 in Appendix C.

2.8.8 Calibration of soil properties

In order to account for site variability, the properties obtained from CPT 022 and CPT 065 (Table 3) are assessed, and based on engineering judgement representative values are selected and adopted in the numerical analysis (Table 8).

In a coupled analysis, the permeability values should be set to realistic values. Given that the hydraulic conductivity values obtained from CPT correlations are considered as rough estimations, a parametric study is conducted to assess the impact of the hydraulic conductivity values on the results. The output of the parametric study is provided in Appendix C and the adopted values are given in Table 8.

The G values obtained from DPCH 35261 (Table 5) are lower than the values obtained from DPCH 35269 (Table 6). For a better understanding of the impact of the shear modulus on the shear strain profiles, three cases are tested: using the lower range of G values from DPCH 35261, using the higher range of G values from DPCH 35269, and using average G values. The cyclic shear stress of 15 kPa is used for the calibration. The shear strain profiles obtained for the three cases are provided in Figure C. 7 of Appendix C. Further calibration

is conducted on these cases by considering three values of Poisson's ratio: 0.48, 0.45 and 0.40 and the results are given in Figure C. 8 of Appendix C.

The shear strain profile obtained from the case of average G values is in better agreement with the in-situ profile compared to the other two cases. This case is considered for further analysis. An additional Poisson's ratio of 0.35 is checked to assess the impact of lower Poisson's ratio values on the results. Moreover, cyclic shear stresses of 5 and 25 kPa are tested. The results obtained from this analysis are provided in Figure C. 9 of Appendix C. The Poisson's ratio parametric study mostly affects the results obtained for a 15 kPa load. The shear strain profile for a Poisson's ratio of 0.40 and a calibration load of 15 kPa is considered in best agreement with the T-Rex shear strain profiles. Table 8 summarizes the properties used in the unreinforced FD model.

Table 8: Calibrated properties adopted in the unreinforced FD model

Depth (m)	N_{60} (blows/30 cm)	$N_{1,60}$ (blows/30 cm)	Unit weight (kN/m^3)	Friction Angle (deg)	Hydraulic conductivity (m/s)	Shear Modulus G (MPa)	Poisson's Ratio	Young's Modulus E (MPa)
0 - 0.6	10	15	17	42	9E-05	23	0.4	63
0.6 -1	5	10	17	40	6E-07	25	0.4	71
1 - 1.25	5	5	17	35	6E-07	25	0.4	69
1.25 - 1.65	5	5	17	34	2E-05	26	0.4	73
1.65 - 1.9	10	10	19	38	2E-05	34	0.4	95
1.9 - 3.3	10	10	19	37	2E-05	48	0.4	133
3.3 - 10	20	20	19	41	7E-05	48	0.4	133

2.8.9 Results and discussions

The unreinforced FD model developed in this section with the calibrated soil properties (Table 8) predicts the in-situ shear strain profile generated during the top-down shaking with some underestimation of shear strain values as depth increases (Figure 11).

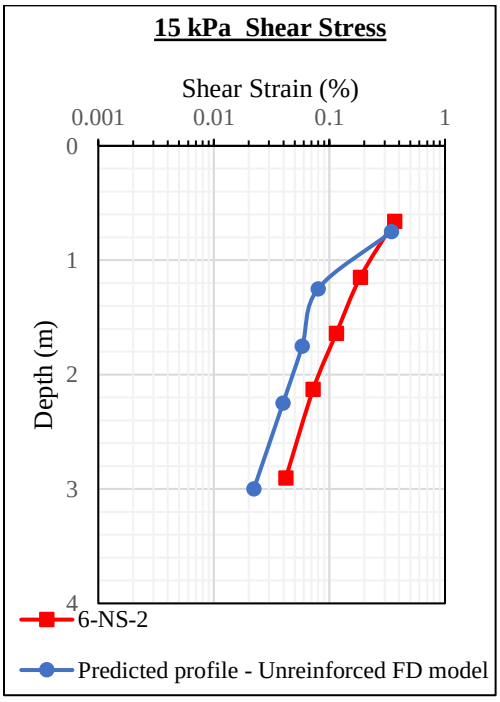

Figure 11: Comparison between the predicted shear strain profile for unreinforced FD model and the in-situ stiffness profile

The r_u histories are plotted at the five control points defined as per section 2.8.7. Figure 12 and Figure 13 compare the r_u histories obtained from the numerical analysis (in red) to the in-situ measurements previously presented in section 2.7.2 (in black) for cyclic shear stresses of 25 and 2.5 kPa respectively. Positive values of r_u represent an increase of the pore water pressure with respect to the existing pressure before the cyclic loading, while negative values represent a drop in pore pressures.

At the shallowest control point (4P) which is at a depth of 0.75 m, the calculated changes in r_u are minimal, almost equal to zero, which differ from the field data. Point 4P is highly influenced by the prescribed hydraulic boundary condition at the ground water level (fixed

at a depth of 0.5 m) above which the pore water pressure is set to zero. Therefore, very small increases in pore pressures occur at point 4P and consequently negligible values of r_u are recorded.

The levels of r_u computed at deeper points are generally comparable to those measured in the field except at the control points 5P for a load of 25 kPa (Figure 12) and 6P for a load of 2.5 kPa (Figure 13) where the numerical values of r_u seem to be underestimated. In general, the computed r_u levels range from 60% to 10% for the case of maximum shear loading and from 2% to 1% for the case of minimum shear loading. Moreover, a decrease of r_u with depth and loading is observed, which is compatible with the field observations. Finally, although the amplitude of the oscillations is generally lower than those observed in the in-situ profiles, the behavior depicted by the numerical r_u histories is fairly comparable with the in-situ behavior.

Finally, the vertical stress, pore pressure and volumetric strain distributions generated by FLAC v.8 are provided in Appendix D. Three different stages are presented:

Stage 1: after application of the gravity loading

Stage 2: after application of the static vertical stress (46 kPa)

Stage 3: after application of the dynamic shear cyclic load (25 kPa and 2.5 kPa)

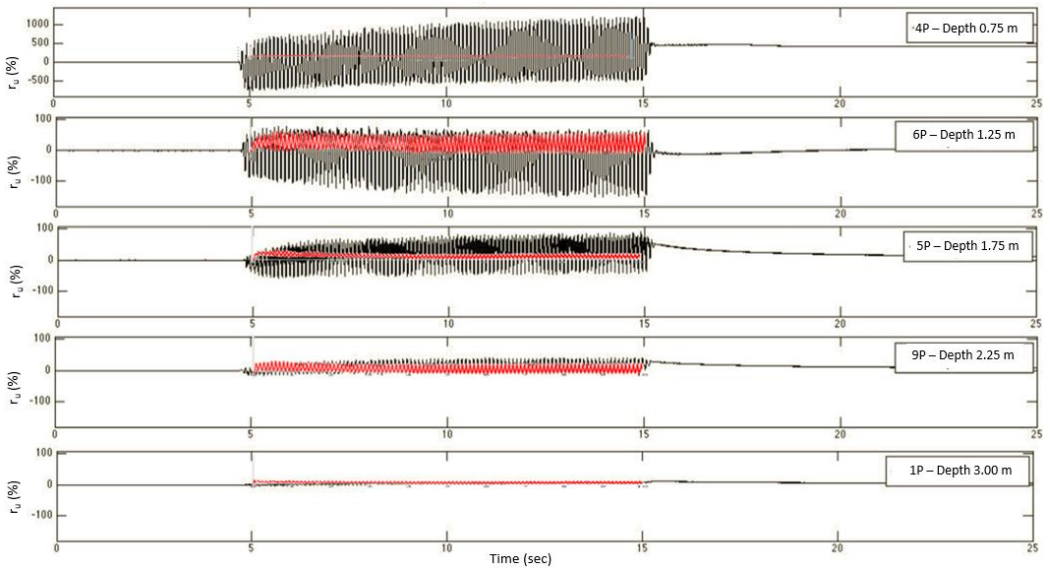

Figure 12: Numerical (red) vs. in-situ (black) r_u histories for a cyclic shear of 25 kPa

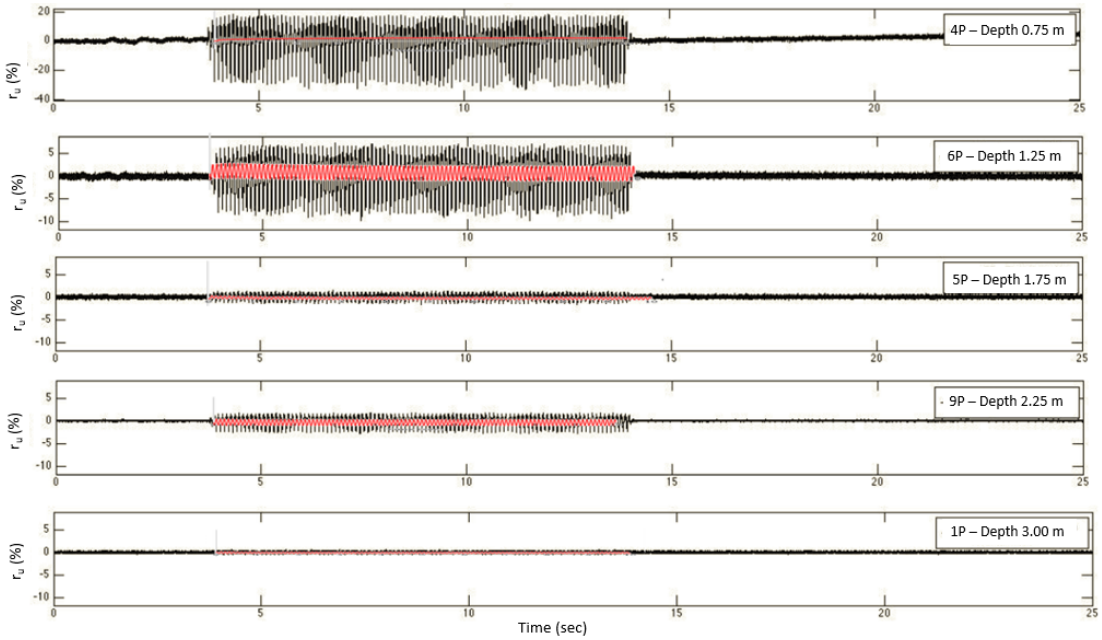

Figure 13: Numerical (red) vs. in-situ (black) r_u histories for a cyclic shear of 2.5kPa

2.9 Reinforced FD Model: Top-Down Shaking

The capability of the model in capturing the improvement in shear strain profiles for reinforced conditions is assessed in this section. RAP elements are introduced to the model while maintaining all remaining variables unchanged. A top-down shaking as described in section 2.8.6 is applied at the surface and the shear strain profiles are plotted and compared to the in-situ results (Figure 9) and to the profiles calculated for unreinforced conditions.

2.9.1 Introduction of RAP elements to the FD model

The RAP elements are introduced to the unreinforced FD model as soil columns with a diameter of 500 mm and a length of 4 m. Two RAP elements are considered, spaced 2 meters center-to-center, introduced under the base plate as shown in Figure 14. The selected dimensions and spacing are compatible with the configuration of the installed RAP columns at the test panel 6-RAP-1 given in Figure 2.

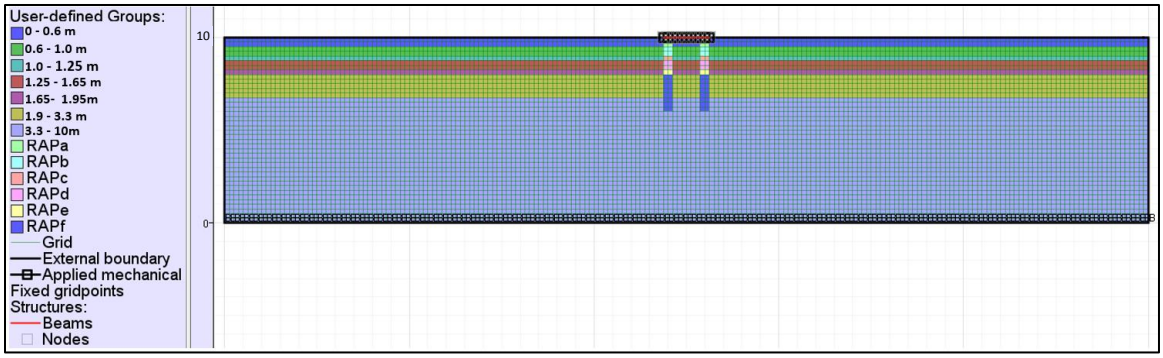

Figure 14: Geometry of the reinforced FD model

The RAP elements are expected to cause an overall improvement at the site. However, as a first conservative approach, no increase in the properties of the soil surrounding the RAP elements is considered and the properties adopted for these soils are as given in section 2.8.8 for unreinforced FD model.

The RAP elements are introduced to the FD model as elastic soil columns. The corresponding elastic properties are determined from DPCH 35279 testing across the RAP gravel piers as given in Table 7. In order to conduct a fully coupled hydro-mechanical analysis, the RAP gravel piers are assigned a hydraulic conductivity value equal to 7E-5 m/s, similar to the value assigned to the sand bottom layer (Table 8). In fact, the RAP elements are stiff piers of crushed aggregates fed and compacted in the cavities. Given the intense compaction process, the hydraulic conductivity is expected to be lower than typical values of gravel material.

2.9.2 Results and discussions

The improvement introduced by the RAP elements is assessed in terms of reduction in shear strains. The shear strain profiles between the RAP elements obtained from the reinforced FD model are compared to the in-situ profile (6-RAP-1) discussed in section 2.7.2 . The results are given in Figure 15a for a cyclic shear load of 15 kPa. The general profile of the predicted shear strains is reasonable, showing an expected decrease in strains with depth due to the decrease in load. The unexplained curvature in the in-situ stiffness profile discussed in section 2.7.2 is not observed in the model output. The in-situ

shear strain values range between 0.02 and 0.06 %, whereas the strain values predicted by the model range between 0.003 and 0.02 %. The FD model therefore tends to underestimate the shear strain values and might be considered to overpredict the improvement associated with the RAP reinforcement. Modeling a 3D problem in 2D frame could induce unrealistic stiffness, providing one possible explanation for the underprediction in shear strains.

A further comparison between the output from the reinforced and unreinforced models is provided in Figure 15b. Given that numerical inputs are identical between the two models, the improvement in the predicted shear strains due to the introduction of the RAP columns is assessed. Figure 15b shows a clear decrease in the stiffness profile for the reinforced model. The median percent change in shear strain with respect to natural conditions is however calculated to be around 85 % which is greater than the values provided in literature (55% change for test panel 6-RAP-1 (Roberts 2017)).

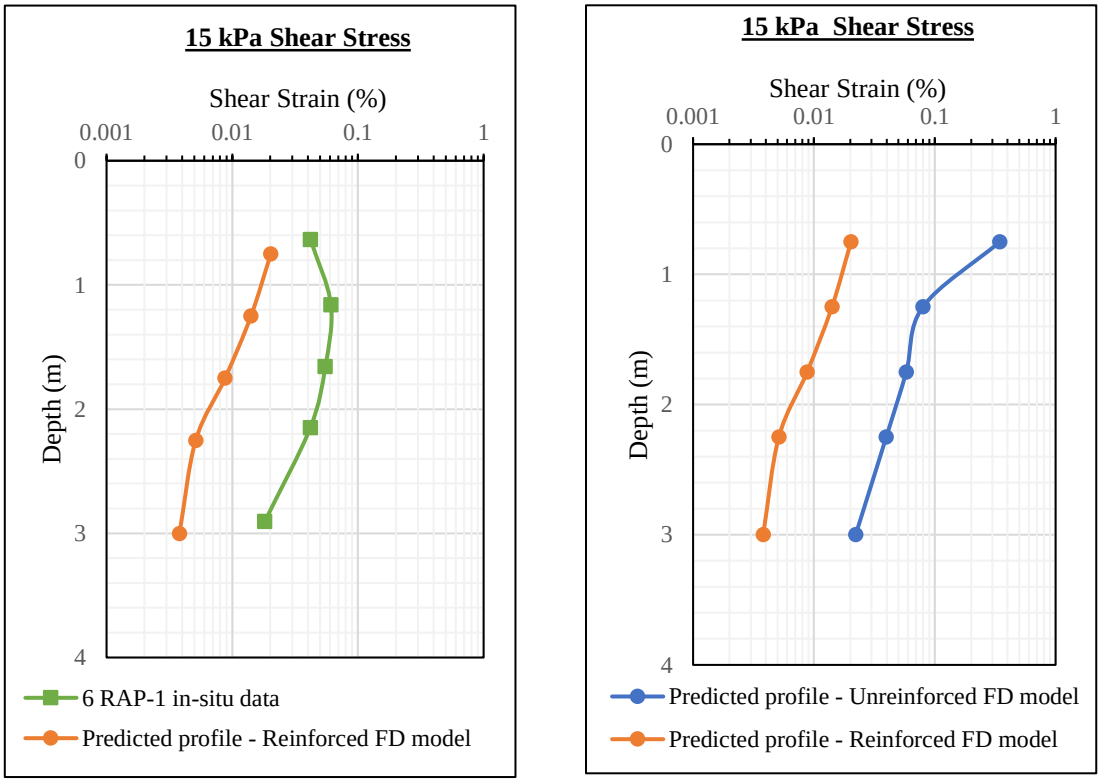

(a) **(b)**

Figure 15: Comparison between the predicted shear strain profile between the RAP elements for reinforced FD model and (a) the in-situ measured profile (6-RAP-1); (b) the predicted profile for unreinforced FD model

2.10 FD models: Bottom-Up Shaking

The FD models are further assessed to preliminary evaluate their capabilities in capturing the response of liquefiable soil during earthquake shaking. The models' characteristics are kept unchanged but the stresses simulating the T-Rex shaking are replaced by a bottom-up shaking applied at the base of the model. Unreinforced and reinforced conditions are tested and the corresponding r_u and shear strain profiles are analyzed.

2.10.1 Selection of shaking motion

The 4 September 2010, M_w7.1 Darfield earthquake is considered for the analysis. Figure 16 provides the locations of the strong motion station (SMS) sites operated in Christchurch area in proximity to Site 6. Different degrees of liquefaction are observed at the SMS sites (Wotherspoon et al. 2014, Markham et al. 2015). The North New Brighton School (NNBS) site did not show manifestations of liquefaction (Wotherspoon et al. 2014), and is the nearest to Site 6 (Figure 16). Therefore, the surface acceleration history recorded at NNBS is downloaded from the PEER Ground Motion Database (https://ngawest2.berkeley.edu/) and used in the analysis. The recorded peak ground acceleration at NNBS for the considered event is equal to 0.21 g.

Figure 16: SMS sites in Christchurch area in proximity to Site 6

2.10.2 Deconvolution of shaking motion

The shaking input motion needs to be applied at the bottom of the 10-meter height FD model. A linear elastic analysis is therefore performed in Strata to calculate the acceleration time history at a depth of 10 m below the ground surface. The V_s profile required for the analysis is estimated using the Christchurch specific CPT-V_s correlation (McGann et al. 2014) and is provided in Appendix E. The surface acceleration time history is applied as an outcrop motion at the top of a 1D soil column and the required history at 10-meter depth is calculated in Strata (Figure 17). The computed acceleration history shows a slight decrease in values compared to the surface acceleration history.

Site 6 is located in the Eastern part of Christchurch where the Riccarton Gravel is deep, occurring between 45 and 50 m below ground surface (Wotherspoon et al. 2014). For the area under consideration, the available CPT soundings extended around 40 m below the ground surface without however encountering the Riccarton Gravel layer. Therefore, in the current deconvolution analysis, the Riccarton Gravel layer was not used as the half-space, which could be impacting the results. Further investigations might be required to refine the deconvolution process and achieve better estimations of the required acceleration time history.

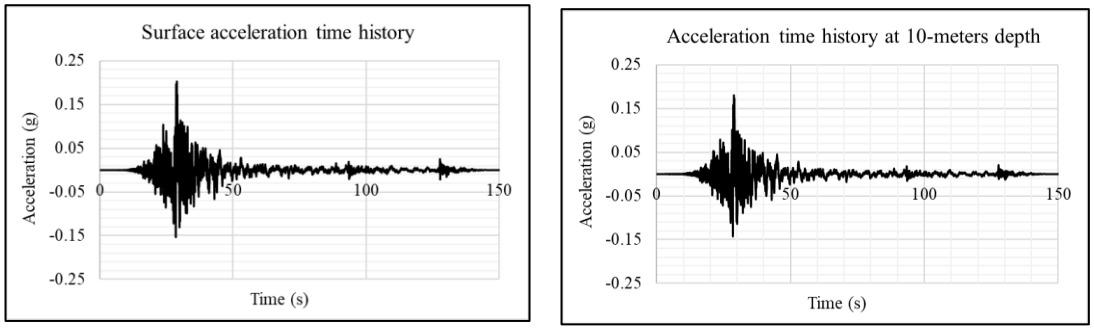

(a) **(b)**

Figure 17: Acceleration time histories (a) at surface; (b) at 10-meters depth

2.10.3 Application of shaking load in FLAC

When a dynamic analysis is conducted in a FLAC model with a compliant base, an acceleration time history cannot be directly applied at the base because it nullifies the effect of the quiet boundary. Instead, it should be transformed into a shear stress history (FLAC manual). The process, following the procedure outlined in Mejia and Dawson (2006), consists first on calculating the upward propagating acceleration, equal to half the outcrop wave obtained from the deconvolution method, then integrating that acceleration to obtain the upward propagating velocity (v_{su}). The shear stress (τ_s) is then computed as:

$$\tau_s = 2\rho V_s v_{su}$$

where ρ is the density of the base material and V_s is the shear velocity at the boundary.

The upward propagating acceleration and v_{su} histories are computed following the above procedure and are provided in Figure 18. For completion, the displacement histories are also included. No permanent drift is recorded for either the velocity or the displacement histories. Beyond 40 seconds of shaking, the accelerations and velocities drop to minimal values. Therefore, in order to avoid unnecessary computational time, the analysis is only run for 40 seconds.

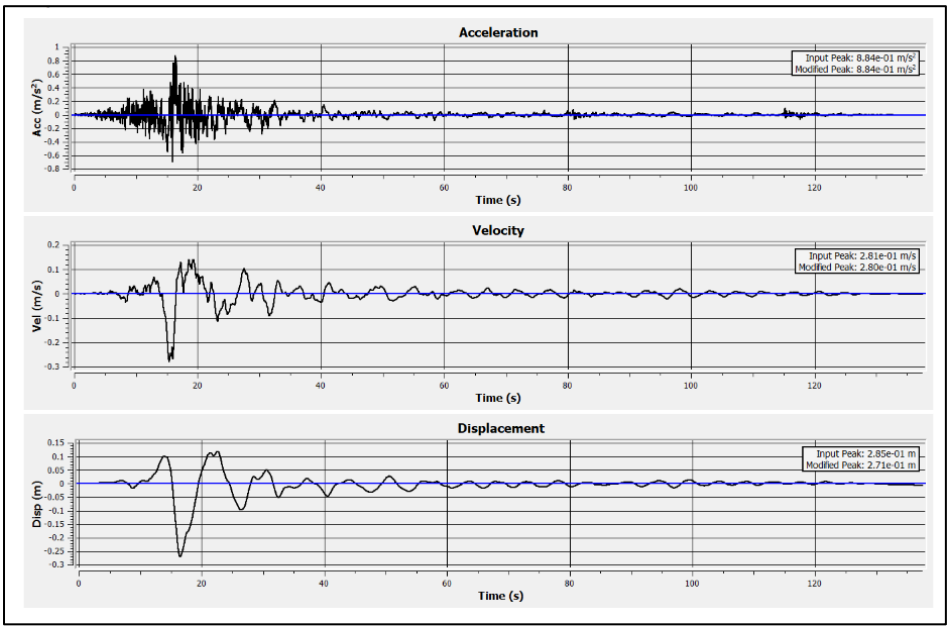

Figure 18: Computed acceleration, velocity and displacement histories

2.10.4 Results and discussion

Figure 19 provides the r_u distribution at the end of shaking for the unreinforced model. The r_u values recorded between the depths of 1 m and 3 m are above 0.5 with a maximum value of 0.7 obtained between 1 and 2 m depth. The values then decrease with depth until reaching a value of 0.1 at 10 m depth.

The results from the simplified liquefaction procedure and the LPI and LPI_{ish} indices (which are in accord with post-earthquake observations) suggested that the upper soil layers are highly susceptible for liquefaction. Consequently, the predicted r_u values from the unreinforced FD model were expected to exceed 1 for these layers. Although the r_u distribution show higher values for the upper layers (above 3 m depth), a unity value is not reached, indicating that the soil does not liquefy under the applied shaking. Therefore, the FD model seems to underestimate the liquefaction potential and underpredict the impact of the shaking.

Figure 20 provides the r_u distribution for the reinforced model. It clearly indicates a decrease in r_u especially between the RAP elements for the upper 3 m, where the values drop from 0.5 and 0.7 to around 0.3. The r_u distribution reflects the improvement introduced by the RAP column. However, given the previously discussed limitations of the FD model, quantitative assessment of the improvement is not yet possible.

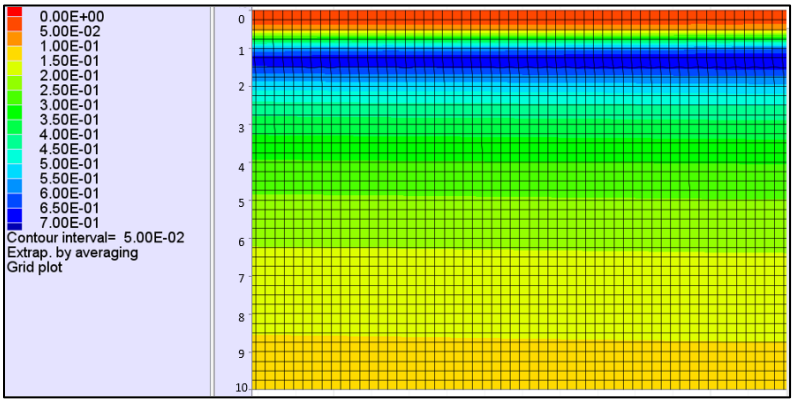

Figure 19: Predicted r_u distribution for bottom-up shaking - unreinforced FD model

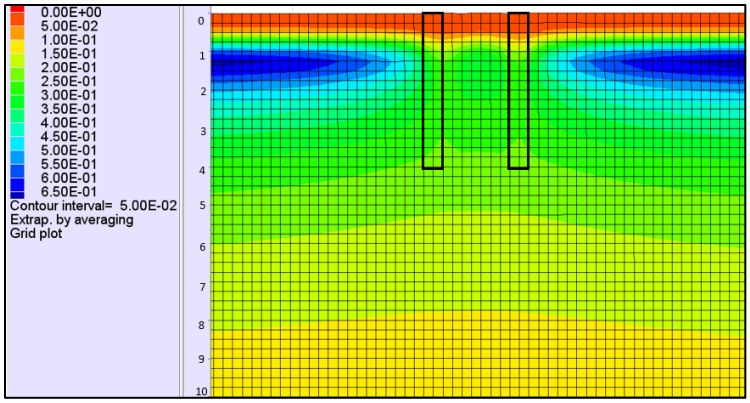

Figure 20: Predicted r_u distribution under bottom-up shaking -reinforced FD model

The variation of r_u with time is plotted at the control points defined as per section 2.8.7 and representative results are provided for the control point 6P (Figure 21). The history obtained from the reinforced model suggests a decrease in the r_u peak value as well as in the value recorded at the end of the 40-seconds shaking compared to unreinforced conditions. However, the general variations in the r_u histories do not show common trends and further investigations are required to understand the reasons behind the observed behavior.

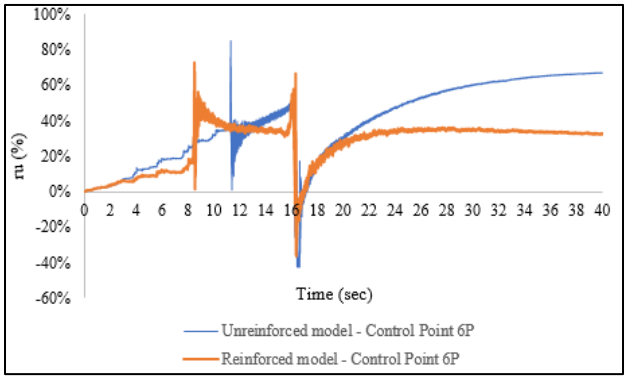

Figure 21: Comparison between the predicted r_u histories at 6P obtained from unreinforced and reinforced models for bottom-up shaking

The improvement introduced by the RAP reinforcement is further assessed in terms of reduction in shear strains. The shear strain profiles obtained between the RAP elements as well as at the boundary of the RAP column are compared to the profile obtained for unreinforced soil (Figure 22).

The shear strain profile computed at the boundary of the RAP elements shows a reduction in values compared to the unimproved soil especially for the upper 2 m. This reduction is not as pronounced for the shear strains recorded between the RAP elements where a significant reduction in shear strains only occurs between a depth of 1 m and 2 m.

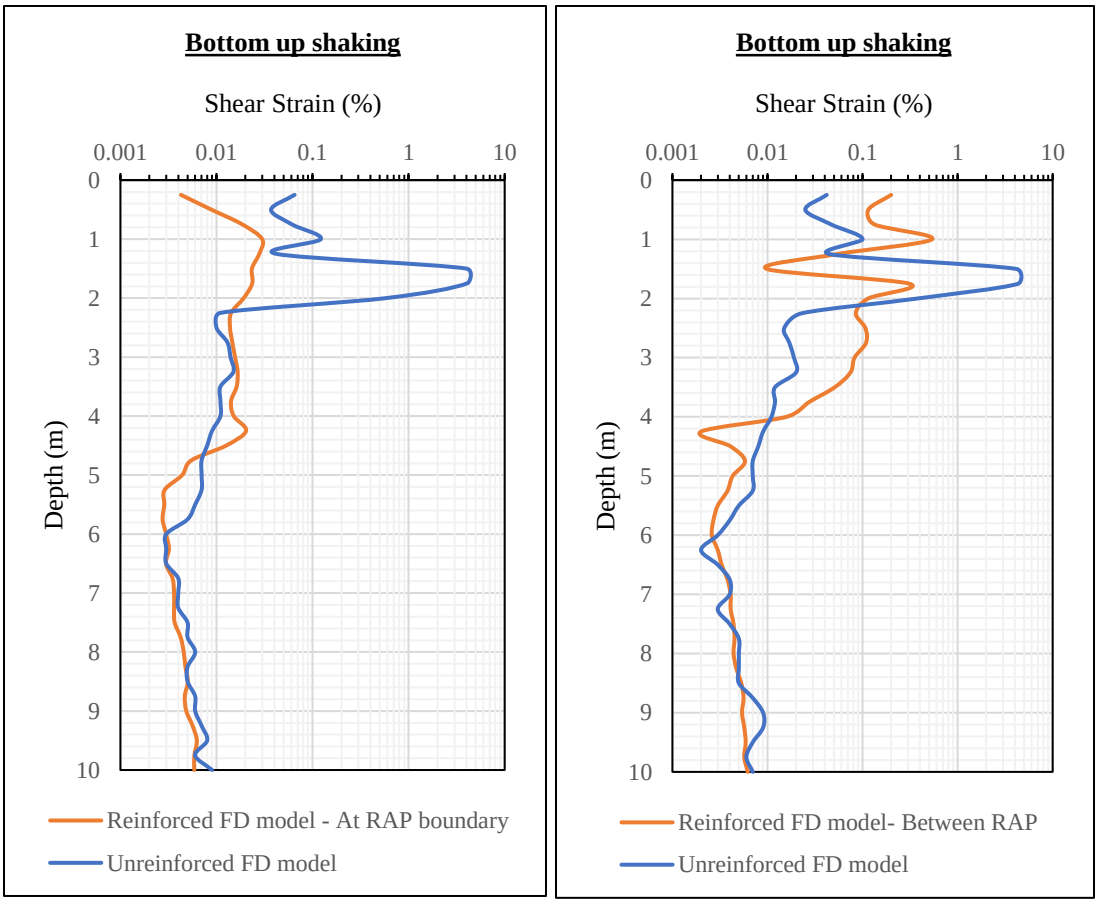

(a) **(b)**

Figure 22: Comparison between the predicted shear strain profile for unreinforced FD model and reinforced model (a) at RAP boundary; (b) between the RAP elements

2.11 Discussion

Under a top-down shaking identical to the in-situ T-Rex shaking, the shear strain and r_u results predicted by the FD model for unreinforced and reinforced conditions show generally acceptable profiles, fairly comparable to the in-situ measurements. The FD models succeed in qualitatively reproducing the overall behavior, indicating an

improvement in soil conditions with the introduction of RAP reinforcement. The general framework adopted in developing the models is therefore valid and better predictability is expected to be achieved with further investigations and refinements. The underestimation in the shear strain profiles currently obtained from the FD models causes an under prediction of the impact of shaking and should be adjusted for to improve the capability of the FD model in predicting liquefaction potential under earthquake motions. Possible causes for the discrepancy between the model outputs and the measured profiles could be attributed to the selected constitutive material model. Although the Byrne (1991) formulation incorporated in the Finn model is widely used in the field, the selection of a more advanced model may be more appropriate to simulate the complexity of the mechanism. Realistic prediction of soil deformation is highly dependent on the stress-strain characteristics of the soil. Soils exhibit a nonlinear and inelastic behavior which makes the stress-strain characteristics extremely complex (Duncan et al. 1980). Targeting the nonlinear behavior of the soil by using hyperbolic constitutive models would be the next step to better understand the mechanics of the problem and increase the predictability level of the FD model.

2.12 Conclusion

The effectiveness of ground improvement methods to mitigate earthquake induced liquefaction is an important area of study. Validation techniques such as in-situ testing, full scale field testing, and field observations offer valuable information. However, advanced numerical modelling can provide insights into the liquefaction response of improved ground that cannot be obtained by more global validation approaches. Calibrating and validating a numerical model that can accurately predict liquefaction hazard requires a complete database, such as the one compiled from the Christchurch trial program that followed the 2010-2011 Canterbury, New Zealand, Earthquake Sequence (CES). Cone penetration testing, direct-push crosshole testing, and T-Rex shaking were conducted both at improved and unimproved soil panels. The conclusions obtained from the in-situ testing program highlight the improvement introduced by the stiff RAP elements and the effectiveness of this technique in reducing liquefaction susceptibility.

The focus of this study is on Site 6. The Green et al. (2018a) CPT-based simplified liquefaction procedure and the LPI and LPI_{ish} frameworks predict the high liquefaction potential of the top 4 to 5 meters of this site, unimproved. Model calibration, thoroughly relying on the Christchurch testing database, is conducted for developing numerical analyses in agreement with in-situ conditions and capable of predicting in-situ behavior. A coupled analysis is performed in a finite difference interface for pre- and post-improvement site conditions applying a top down shaking identical to the in-situ T-Rex vibration. The Byrne (1991) formulation widely used in the field and incorporated in the Finn constitutive model is adopted in the analysis. The numerical results show a significant decline in shear strains for reinforced conditions emphasizing the improvement introduced by the RAP elements. Although the predicted results show generally acceptable trends, the FD models seem to underestimate the shear strain and r_u values. Consequently, when a bottom-up shaking similar to the one introduced by the 4 September 2010 Darfield earthquake was applied, the FD model under predicted the severity level of liquefaction observed at Site 6. Further investigations to better account for the problem complexity by incorporating a more appropriate constitutive model are expected to achieve better predictability levels. After that, the advanced FD modelling will provide insights into the liquefaction response of the improved ground to a range of shaking intensities and footing loads. This will contribute to a better understanding of the soil behavior when reinforced with RAP elements under different layouts, which will be essential to determine the efficiency of this soil reinforcement approach in mitigating liquefaction hazard.

References

Baldi, G., Bellotti, R., Ghionna, V.N., Jamiolkowski, M., and Lo Presti, D.F.C., (1989). "Modulus of sands from CPTs and DMTs." *Proc. 12th Int. Conf. on Soil Mechanics and Foundation Engineering*. Rio de Janeiro. Balkema Pub., Rotterdam, Vol.1, pp. 165-170.

Bradley, B.A. (2013). "Site-specific and spatially-distributed ground motion intensity estimation in the 2010-2011 Christchurch earthquakes." *Soil Dynamics and Earthquake Engineering*, 48:35-47.

Bradley, B.A. (2017). "On-going challenges in physics-based ground motion prediction and insights from the 2010-2011 Canterbury and 2016 Kaikōura, New Zealand earthquakes." *Proc. Australian Earthquake Engineering Society (AEES) Annual Conference*. Canberra, Australia. 23pp.

Byrne, P.M. (1991). "A Cyclic Shear-Volume Coupling and Pore-Pressure Model for Sand," *Proc. 2nd Int. Conf. on Recent Advantages in Geotechnical Earthquake Engineering and Soil Dynamics*, St Louis, Missouri.

Duncan, J.M., Byrne, P., Wong, K.S., and Mabry, P. (1980). "Strength, Stress-Strain and Bulk Modulus Parameters for Finite Element Analyses of Stresses and Movements in Soil Masses." Report No. USB/GT/80-01, University of California, Berkeley.

Eseller-Bayat, E., Yegian, M.K., Alshawabkeh, A., and Gokyer, S. (2009). "A New Mitigation Technique for Preventing Liquefaction-induced Bluilding Damages During Earthquakes." *Proc. Earthquake & Tsunami WCCE-ECCE -TCCE Joint Conference*, Istanbul, Turkey, June 22-24, 2009, 8pp.

FLAC v.8 Manual. www.itascacg.com

Green, R.A., Bommer, J.J., Rodriguez-Marek, A., Maurer, B., Stafford, P., Edwards, B., Kruiver, P.P., de Lange, G., and van Elk, J. (2018a). "Assessing the Liquefaction Hazard in the Groningen Region of the Netherlands due to Induced Seismicity: Limitations of Existing Procedures and Development of a Groningen-Specific Framework." *Bulletin of Earthquake Engineering*.

Green, R.A., Maurer, B.W., and van Ballegooy, S. (2018b). "The Influence of the Non-Liquefied Crust on the Severity of Surficial Liquefaction Manifestations: Case History from the 2016 Valentine's Day Earthquake in New Zealand," *Proc. Geotechnical Earthquake Engineering and Soil Dynamics V* (GEESD V), Austin, TX.

Hausler, E.A. and Sitar, N. (2001). "Performance of soil improvement techniques in earthquakes." *Proc 4th Int. Conf. on Recent Advances in Geotechnical Earthquake Engineering and Soil Dynamics*, Paper No. 10.15.

Ishihara, K. (1985). "Stability of natural deposits during earthquakes." *Proc. 11th Int. Conf. on Soil Mechanics and Foundation Engineering*, 1, San Francisco, CA, 321-376.

Iwasaki, T., Tatsuoka, F., Tokida, K., and Yasuda, S. (1978). "A practical method for assessing soil liquefaction potential based on case studies at various sites in Japan." *Proc. 2nd Int. Conf. on Microzonation*, San Francisco, CA, USA, 885-896.

Jamiolkowski, M., Ladd, C.C., Germaine, J.T., and Lancellotta, R., (1985). New developments in field and laboratory testing of soils. *Proc 11th Int. Conf. on Soil Mechanics and Foundation Engineering*. San Francisco, California, August 1985, Vol.1 pp. 57-153.

Jefferies, M.G., and Davies, M.P., (1993). "Use of CPTU to estimate equivalent SPT N_{60}". *Geotechnical Testing Journal*, ASTM, 16(4): 458-468.

Kramer, S.L. (1996). *Geotechnical Earthquake Engineering*. Prentice Hall, Upper Saddle River, N.J.

Kulhawy, F.H., and Mayne, P.H., (1990). *Manual on Estimating Soil Properties for Foundation Design*, Report EL-6800 Electric Power Research Institute, EPRI.

Lysmer, J. and Kuhlemeyer, R.L. (1969). "Finite Dynamic Model for Infinite Media," *J. Eng. Mech., 95*(EM4), 859-877.

Markham, C.S., Bray, J.D., and Macedo, J. (2015). *Proc 6th Int. Conf. on Earthquake Geotechnical Engineering*. Christchurch, New Zealand, 1-4 November 2015.

Martin, G.R., Finn, W.D., and Seed, H.B. (1975). "Fundamentals of Liquefaction under Cyclic Loading," *J. Geotech., Div*. ASCE, 101(GT5), 423-438.

Maurer, B.W., Green, R.A., and Taylor, O.D. (2015). "Moving towards an Improved Index for Assessing Liquefaction Hazard: Lessons from Historical Data." *Soils and Foundations*, 55(4): 778–87.

McGann, C., Bradley, B., Taylor, M., Wotherspoon, L., and Cubrinovski, M. (2014). "Development of an empirical correlation for predicting shear wave velocity of Christchurch soils from cone penetration test data." *Soil Dynamics and Earthquake Engineering*, 00(0), 15–27.

Mejia, L.H. and Dawson, E.M. (2006). "Earthquake deconvolution for FLAC". *4th International FLAC Symposium on Numerical Modeling in Geomechanics*. Minneapolis,2006

Mitchell, J.K., Baxter, C.D.P., and Munson, T.C. (1995). "Performance of improved ground during earthquake." *Soil Improvement for Earthquake Hazard Mitigation* (R.D. Hryciw, ed.), ASCE GSP 49, 1-36.

Mitchell, J.K. and Martin, J.R. (2000). "Performance of improved ground and earth structures." *Earthquake Spectra,* 16(Supplement A): 191-225.

New Zealand Geotechnical Database. www.nzgd.org.nz

Peck, R.B., Hanson, W.E., and Thornburn, T.H., (1974). *Foundation Engineering, 2nd ed.*, John Wiley and Sons, New York, NY

PEER Ground Motion Database. www.ngawest2.berkeley.edu/

Roberts, J.N. (2017). "Field Evaluation of Large-Scale, Shallow Ground Improvements to Mitigate Liquefaction Triggering." MS Thesis, Department of Civil, Architectural, and Environmental Engineering, University of Texas, Austin, TX.

Robertson, P.K., and Campanella, R.G., (1983a). "Interpretation of cone penetration tests – Part I (sand)". *Canadian Geotechnical Journal*, 20(4): 718-733.

Robertson, P.K. and Wride, C.E. (1998). "Evaluating Cyclic Liquefaction Potential Using the Cone Penetration Test." *Canadian Geotechnical Journal,* 35(3): 442–59.

Robertson, P.K., (2009a). "Interpretation of cone penetration tests – a unified approach." *Canadian Geotechnical Journal,* 46:1337-1355.

Robertson, P.K. and Cabal, K.L. (2015). *Guide to Cone Penetration Testing for Geotechnical Engineering.* 6th Edition. Gregg Drilling & Testing, Inc.

van Ballegooy S., Cox S.C., Thurlow C., Rutter H.K., Reynolds T., Harrington G., Fraser J., and Smith T. (2014). "Median water table elevation in Christchurch and surrounding area after the 4 September 2010 Darfield earthquake: Version 2." GNS

Science Report 2014/18, Institute of Geological and Nuclear Sciences Limited, New Zealand.

van Ballegooy, S., Roberts, J.N., Stokoe, K.H., Cox, B., Wentz, F., and Hwang, S. (2015). "Large scale testing of ground improvements using controlled, dynamic staged loading with T-Rex." *Proc. 6th Int. Conf. on Earthquake Geotechnical Engineering* (6ICEGE), Christchurch, New Zealand, 2-4 November.

Wentz, F., van Ballegooy, S., Rollins, K., Ashford, S., and Olsen, M. (2015). "Large scale testing of shallow ground improvements using blast-induced liquefaction." *Proc. 6th Int. Conf. on Earthquake Geotechnical Engineering* (6ICEGE), Christchurch, New Zealand, 2-4 November.

Wissmann, K., van Ballegooy, S., Metcalfe, B., Dismuke, J., and Anderson, C. (2015). "Rammed aggregate pier ground improvement as a liquefaction mitigation method in sandy and silty soils." *Proc. 6th Int. Conf. on Earthquake Geotechnical Engineering* (6ICEGE), Christchurch, New Zealand, 2-4 November.

Woeste, D., Green, R.A., Rodriguez-Marek, A. and Ekstrom, L., (2016). "A review of Verification and Validation of Ground Improvement Techniques for Mitigating Liquefaction." *Center for Geotechnical Practice and Research*. Report No.86. Virginia Tech, Blacksburg, Virginia.

Wotherspoon, L., Orense, R., Jacka, M., Green, R.A., Cox, B., and Wood, C., (2014). "Seismic Performance of Improved Ground Sites during the Canterbury Earthquakes." *Earthquake Spectra*, 30(1), 111-129.

Wotherspoon, L., Orense, R., Bradley, B.A., Cox, B., Wood, C. and Green, R.A. (2014). "Geotechnical characterization of Christchurch strong motion stations." *Earthquake Commission Biennial Grant Report*, Project No. 12/629.

Youd, T.L., Idriss, I.M., Andrus, R.D., Arango, I., Castro, G., Christian, J.T., Dobry, R., Finn, W.D.L., Harder, L.F., Hynes, M.E., Ishihara, K., Koester, J., Liao, S., Marcuson III, W.F., Martin, G.R., Mitchell, J.K., Moriwaki, Y., Power, M.S., Robertson, P.K., Seed, R.B., and Stokoe II, K.H., (2001). "Liquefaction resistance of soils: Summary report from the 1996 NCEER and 1998 NCEER/NSF workshop on evaluation of liquefaction resistance of soils." *Journal of Geotechnical and Geoenvironmental Engineering*, 127(10): 817-833.

Ziotopoulou, K., and Boulanger, R.W. (2015). "Validation Protocols for Constitutive Modeling of Liquefaction." *Proc. 6th Int. Conf. on Earthquake Geotechnical Engineering* (6ICEGE), Christchurch, New Zealand, 1-4 November.

Chapter 3: Thesis Conclusions

3.1 Summary

The main objective of this thesis was to compile a database of pre- and post-treatment in-situ data and use the data to calibrate a finite difference numerical model that can be used to predict liquefaction response under a wide range of loading conditions. A description of the field testing program performed at Christchurch, New Zealand, following the 2010-2011 Canterbury Earthquake Sequence with a special emphasis on the RAP-reinforced test panel was first provided. The data were then used to evaluate the liquefaction potential at Site 6 using Green et al. (2008a) procedures and to estimate the geotechnical and elastic properties of soil materials at pre- and post-improvement test panels. Later, the study expands on the development and calibration of an unreinforced finite difference model in FLAC. The model characteristics including the definition of geometry, boundary conditions, mechanical constitutive model and loading stages were thoroughly discussed. The results obtained for unimproved conditions were presented, then the RAP elements were introduced to the model and the consequent improvement in results was assessed. The key findings from this work are provided in the next section.

3.2 Key Findings

Developing a numerical model that can predict the dynamic response of soils and the liquefaction triggering under realistic seismic shakings is a complex problem that requires thorough and careful examination. The finite difference technique performed in a FLAC platform is a powerful tool capable of modeling coupled stress-flow situations and simulate large deformation problems. However, before attempting to apply realistic bottom-up seismic shaking, an extensive calibration process against experimental and/or field data is crucial to achieve reliable results. In an attempt to simplify the problem, the Finn model that incorporates the widely used Byrne (1991) formulation is adopted. The FD simulation showed lower shear strains for RAP reinforced soil compared to natural soils as observed on site, but the predicted improvement was slightly overestimated. Despite the thorough calibration efforts, the models only succeed in qualitatively reproducing the general overall

behavior without quantitatively matching the in-situ values for shear strains and r_u. The discrepancy could be attributed to the selected constitutive model. Therefore, in numerical modeling, the complexity of a problem should be tackled in stages, and different aspects of the problem should be addressed separately. Starting with a simplified approach is important to understand the fundamentals of the problem, then building up complexity levels should follow to achieve an overall understanding of the mechanism and account for the complexity of the site conditions. Further investigations are therefore required to refine the model and increase its capacity in predicting the in-situ results for top-down shaking. Switching to more complex constitutive models would be the next step before applying realistic bottom-up earthquake shakings.

3.3 Recommendations for Future Work

The FD models developed in the current study underestimate the shear strains generated in liquefiable soils subjected to top-down shakings and overestimate the improvement in soil response due to RAP reinforcement. In an attempt to increase the predictability of the models, recommendations for extended research include:

- Use the hyperbolic constitutive model (Duncan et al. 1980) to account for the non-linearity of the soil stress-strain characteristics and recalibrate the soil properties.
- For the reinforced FD analysis, after switching to the hyperbolic constitutive model, calibrate the properties of the RAP elements as well as those of the surrounding soils. The introduction of the RAP elements is expected to improve the overall conditions at the site. However, in the current FD model, the properties of the soil surrounding the RAP columns were initially kept equal to the properties adopted in the unreinforced model, and given that the predicted shear strains were already underestimated, no later improvement to these properties was considered.
- Investigate the equivalence between 2D and 3D numerical simulations and modify the dimension of RAP elements and the hydraulic conductivity values accordingly.
- Investigate the deconvolution methods to accurately calculate the acceleration time histories that should be applied at the bottom boundary of the model for assessing the liquefaction potential.

Appendix A: Evaluation of the Liquefaction Potential: Site 6

Appendix A provides the details of the liquefaction analysis conducted at Site 6. The analysis is conducted using the Green et al. (2018a) CPT-based simplified liquefaction triggering procedure. The CPT data is obtained from the New Zealand Geotechnical Database (www.nzgd.org.nz). This appendix provides the estimated median a_{max} values and the water table level at the time of earthquake used in the analysis. The determination of the water table depth at the time of testing is also provided and the results of the liquefaction analysis for the six CPT sounding data for unimproved conditions at Site 6 are presented.

1. Estimation of the earthquake median a_{max}

Two earthquakes from the 2010-2011 Canterbury, New Zealand, Earthquake Sequence (CES) were responsible for much of the widespread liquefaction-related damage. The two earthquakes are:

- The 4 September 2010 Darfield Earthquake with a moment magnitude of 7.1
- The 22 February 2011 Christchurch Earthquake with a moment magnitude of 6.2

The two major earthquakes listed above are considered separately and the factors of safety against liquefaction corresponding to each earthquake are calculated independently.

Two ground motion prediction models, Bradley (2013) and Bradley (2017), were used to estimate the median a_{max} values for each of the earthquakes. For the 4 September 2010, M_w7.1 Darfield Earthquake, the estimated median a_{max} values were 0.182 g and 0.204 g using Bradley (2013) and Bradley (2017) models respectively. For the 22 February 2011, M_w6.2 Christchurch earthquake, the median a_{max} value estimated using Bradley (2013) varied between 0.521 g and 0.525 g for the different CPT locations, whereas it was estimated to be equal to 0.431 g, constant across the entire site, using Bradley (2017) model. Given that the a_{max} values predicted by the two models differ, both values were used in the analyses. Table A. 1 summarizes the different cases used in the analysis.

2. Estimation of the water table levels

Two ground water tables (GWT) should be considered when conducting a liquefaction analysis. The water table depth at the time of earthquake should be used when calculating the CSR* and K_σ factor, whereas the water table depth measured during the CPT testing should be considered when computing the corrected CPT tip resistance defined in Green (2008a) as (q_{c1Ncs}).

2.1. Estimation of the water table at the time of earthquake

The ground water table at the time of the earthquakes was obtained from Van Ballegooy et al. (2014). For the September 4, M_w7.1 2010 Darfield earthquake, the ground water depth varied between 1.351 m and 1.793 m across Site 6, whereas it varied between 1.30 m and 1.833 m for the February 22 2011 M_w6.2 Christchurch earthquake. Both the upper and lower limits of the water table depth were considered in order to account for the variability of the site conditions in the liquefaction analysis, especially for the CPT locations where no direct data was provided (Table A. 1).

Table A. 1: a_{max} and GWT considered for liquefaction analysis

CPT ID Code	4 September 2010, M_w7.1 Darfield Earthquake				22 February 2011,M_w6.2 Christchurch Earthquake			
	a_{max} (g)		GWT* (m)		a_{max} (g)		GWT* (m)	
	Bradley (2013)	Bradley (2017)	Lower limit	Higher limit	Bradley (2013)	Bradley (2017)	Lower limit	Higher limit
CPT 022	0.182	0.204	1.394		0.523	0.431	1.379	
CPT 023	0.182	0.204	1.351	1.793	0.525	0.431	1.3	1.833
CPT 024	0.182	0.204	1.351	1.793	0.525	0.431	1.3	1.833
CPT 025	0.182	0.204	1.578		0.524	0.431	1.527	
CPT 065	0.182	0.204	1.351	1.793	0.521	0.431	1.3	1.833
CPT 079	0.182	0.182	1.351	1.793	0.524	0.431	1.3	1.833

*GWT: The ground water table reported as the depth of water table below the ground level for each CPT location at the time of earthquake

2.2. Estimation of the water table at the time of CPT testing

The level of water at the time of testing was estimated from the CPT sounding data. Figure A. 1 provides sample data downloaded from New Zealand Geotechnical Database (www.nzgd.org.nz) for CPT 023 sounding.

TABULATED CPT DATA		
CPT ID Code:	BEX-TCR01-CPT023	
Address:	18 & 20 Wairoa St	
Project:	EQC TC3 Geotechnical Investigations	
T&T Ref:	52003.2000	
Suburb:	Bexley	
CPT ID No:	2374487	
Test Date:	15-May-2013	
Easting:	2487508.35	mE (NZMG)
Northing:	5744093.47	mN (NZMG)
Elevation:	0.60	MSL (CCC 20/01/12 Datum-9.043)
Located By:	Survey GPS	(Options = 'Survey GPS', 'Hand GPS' or 'Not located')
CPT Operator:	Pro-Drill	
Pre-Drill:	0.0	m below ground level
Assumed GWL:	0.7	m below ground level
Max Depth:	10	m below ground level
Other Testing:		(Options = 'Dissipation' and/or 'Seismic downhole')
Comments:		
Last Updated:	8-Feb-2012	Date of last update of header data

Figure A. 1: GWT at time of CPT testing from the tabulated CPT 023 data (www. nzgd.org.nz)

A simple verification of the provided value of GWT for each CPT sounding was conducted as follows:

- Plotting the pore pressure profile from the CPT data
- Estimating an elevation of the water table
- Plotting the estimated hydrostatic pore pressure linear variation corresponding to the estimated water table elevation.
- Varying the estimated water table elevation in a way to match the estimated hydrostatic pore pressure linear variation with the linear portion of the pore pressure profile
- Verifying that the estimated water table elevation corresponds to the tabulated water table depth.

A sample example of the procedure is provided in Figure A. 2 where the pore pressure profile for CPT 023 as well as the estimated hydrostatic pore pressure linear variation and the corresponding water table level are plotted.

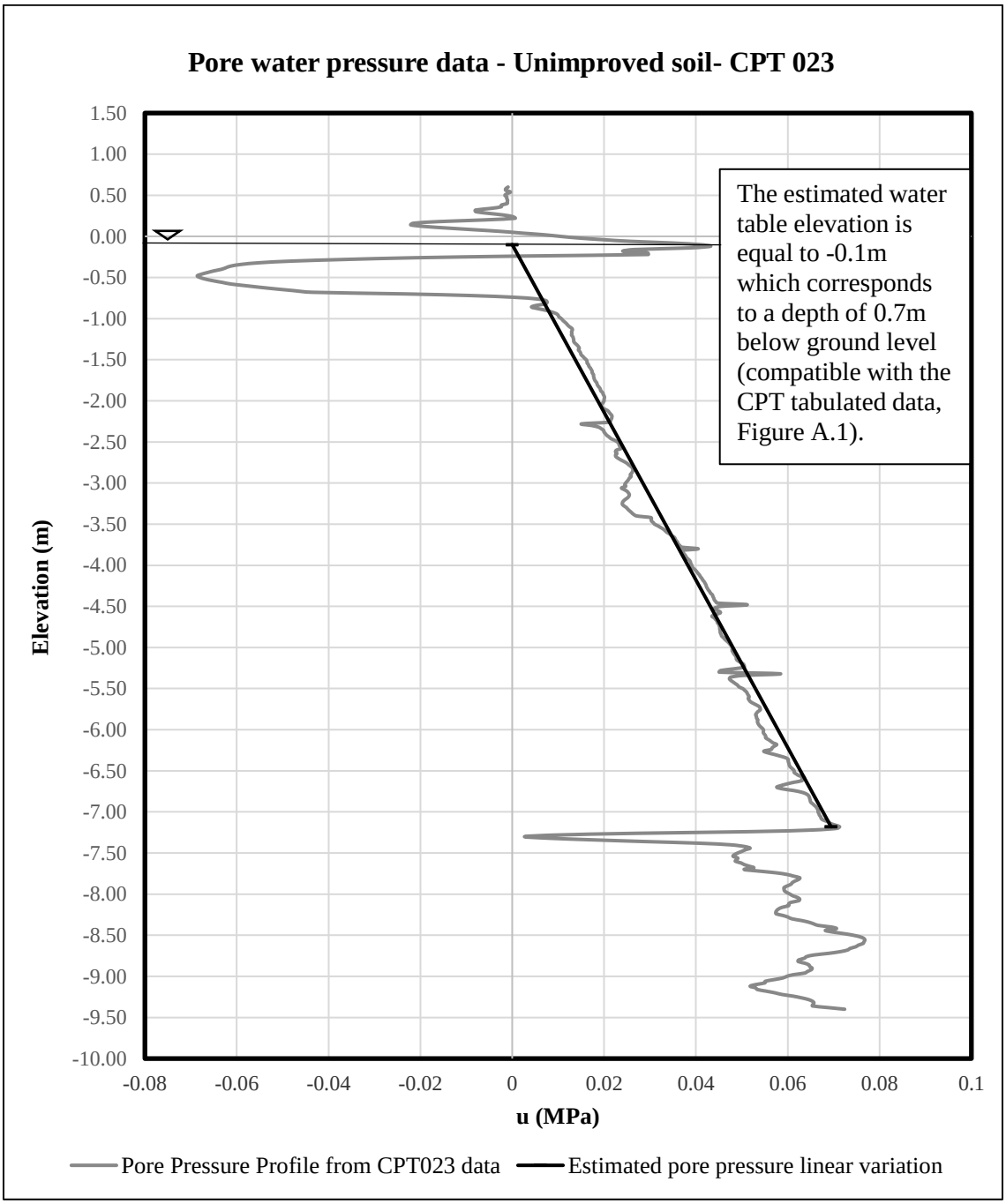

Figure A. 2: Verification of GWT at time of CPT testing for CPT 023

3. Evaluation of the liquefaction potential

The liquefaction potential at Site 6 was assessed for the six CPT sounding data available for unimproved conditions (Figure 1).

For the two acceleration models Bradley (2013) and Bradley (2017) (Table A. 1), only slight variations in the factors of safety were recorded and no major drop in the FS values was encountered at any CPT location. Hereafter, the results corresponding to the highest a_{max} value for each earthquake are only provided.

Both the upper and lower limits of GWT at the time of earthquake are considered (Table A. 1). Representative results of q_{c1Ncs}, Ic, and FS are provided in Figure A. 3 for CPT 065 for the 22 February 2011, M_w6.2 Christchurch earthquake where the GWT at time of earthquake was varied from 1.3 m to 1.833 m. Soils above the water table are considered not to liquefy. Therefore, a shallower water table would result in a thinner non-liquefiable crust and a higher liquefaction potential.

Figure A. 4 summarizes the FS and Ic graphs obtained for the CPT tests conducted in the pre-improved soil at Site 6 for both the 22 February 2011 Christchurch earthquake and the 4 September 2010 Darfield earthquake, considering the highest a_{max} values and the shallower water tables. It is clear that most of the Ic values drop below 2.6 indicating that the soil across Site 6 is highly susceptible for liquefaction, except for thin layers of clayey soil detected at few locations. Similarly, with an adopted threshold of 1, the FS graphs reflect a high potential of liquefaction, especially for the upper layers of soils and the liquefaction hazard is more aggravated for the 22 February 2011 Christchurch earthquake because of the higher induced ground accelerations.

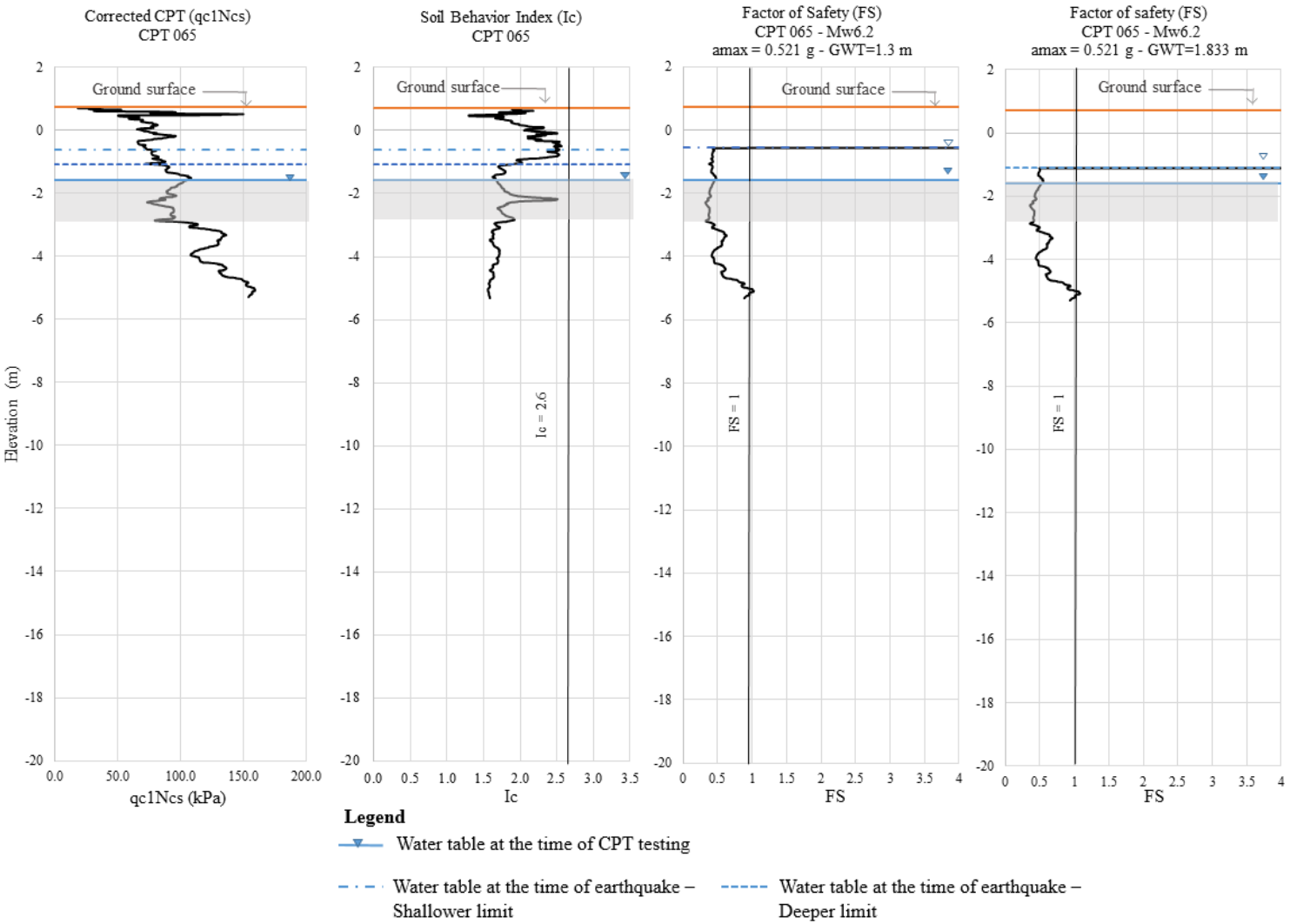

Figure A. 3: q_{c1Ncs}, Ic, and FS for CPT 065 – Mw6.2 & a_{max} = 0.521 g - GWT at time of Earthquake equal to 1.3 m & 1.833 m

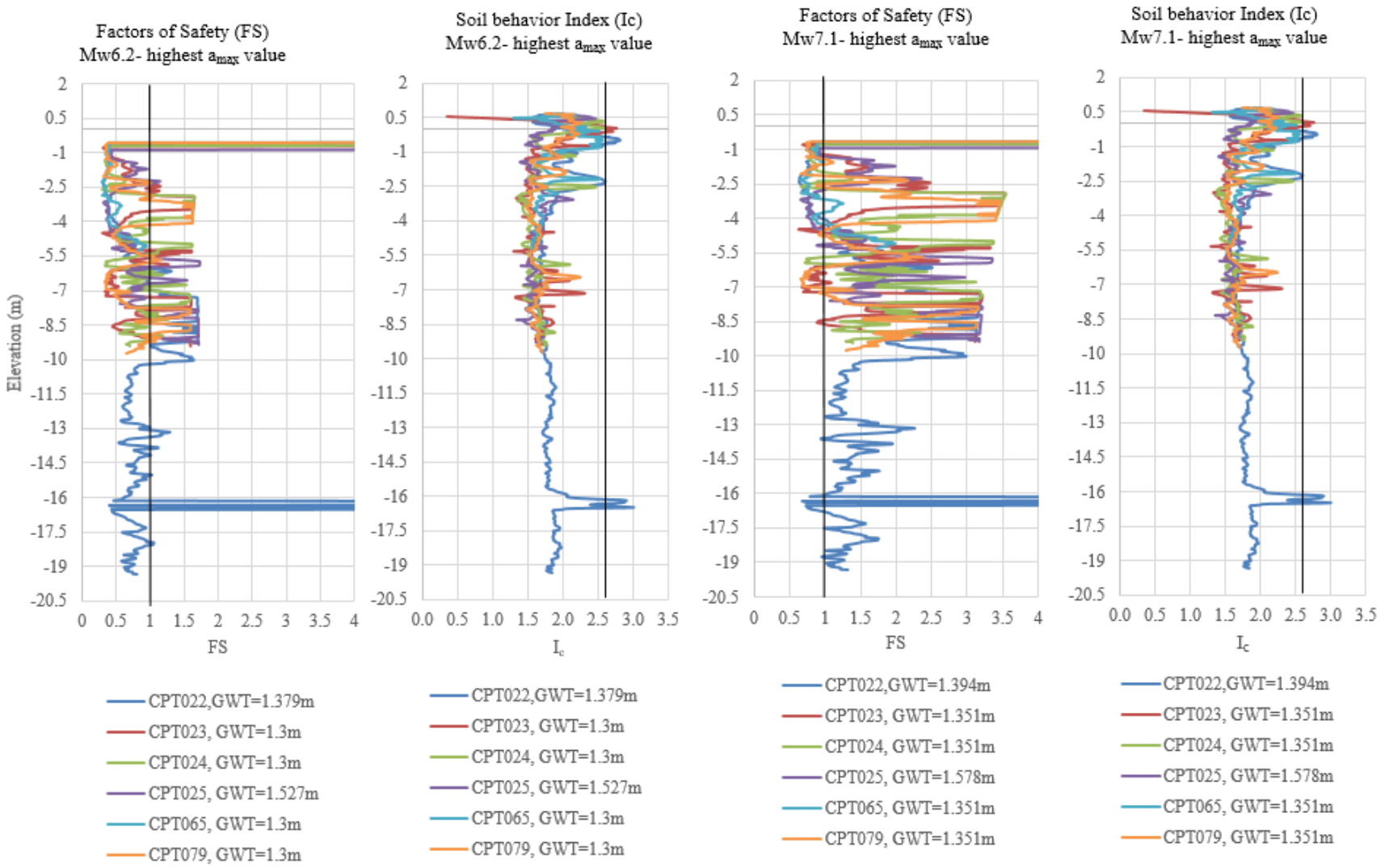

Figure A. 4: FS and Ic profiles for CPT sounding data available for unimproved conditions at Site 6- Mw6.2 and Mw7.1

Appendix B: Estimation of Material Properties from CPT and DPCH Testing

The soil geotechnical parameters are estimated based on CPT soundings. The *Guide to Cone Penetration Testing for Geotechnical Engineering* (Robertson and Cabal 2015) is used as a main reference and the CPT correlations of main interest are summarized in this Appendix. The correlations between the V_s values obtained from the DPCH testing and the elastic properties of the soil are also provided.

1. Estimation of soil properties from semi-empirical CPT correlations

Robertson and Cabal (2015) suggest several correlations to estimate N_{60}, $N_{1,60}$, unit weight, relative density, friction angle, and hydraulic conductivity values of soils from CPT. The layers' identification as well as some of the correlations are related to the soil behavior index Ic and the equivalent clean sand cone penetration resistance defined by Robertson and Cabal 2015 as $(Q_{tn})_{cs}$. Since these correlations are empirical, the parameters used in the equations should be calculated exactly the way defined by the developers of the correlations. Therefore, for consistency, although the Ic and $(Q_{tn})_{cs}$ (defined in Green et al. (2018) as q_{c1Ncs}) were previously determined following Green et al. (2018a) procedures, these values were recalculated using the procedure provided by Robertson and Cabal (2015).

1.1 Soil Behavior Type Index Ic

The Soil Behavior Type Index Ic is estimated using Equation (1.1)

$$Ic = ((3.47 - \log Q_{tn})^2 + (\log F_r + 1.22)^2)^{0.5} \quad (1.1)$$

where:

Q_{tn} = normalized cone penetration resistance calculated using a stress exponent *n* that varies with soil type via Ic (dimensionless)

$$Q_{tn} = \left(\frac{q_t - \sigma_{v0}}{P_a} \right) \left(\frac{P_a}{\sigma'_{v0}} \right)^n$$

F_r = normalized friction ratio (in %)

$= (f_s / (q_t - \sigma_{vo})) \times 100\%$

q_t = corrected tip resistance for pore pressures acting on the cone geometry

In sandy soils, $q_c = q_t$

σ_{v0} = total vertical stress

σ'_{v0} = effective vertical stress

P_a = reference pressure (same units as q_t, σ_{v0} and σ'_{v0})

The determination of Ic depends on the stress exponent *n* and therefore involves an iterative process as shown in Figure B. 1.

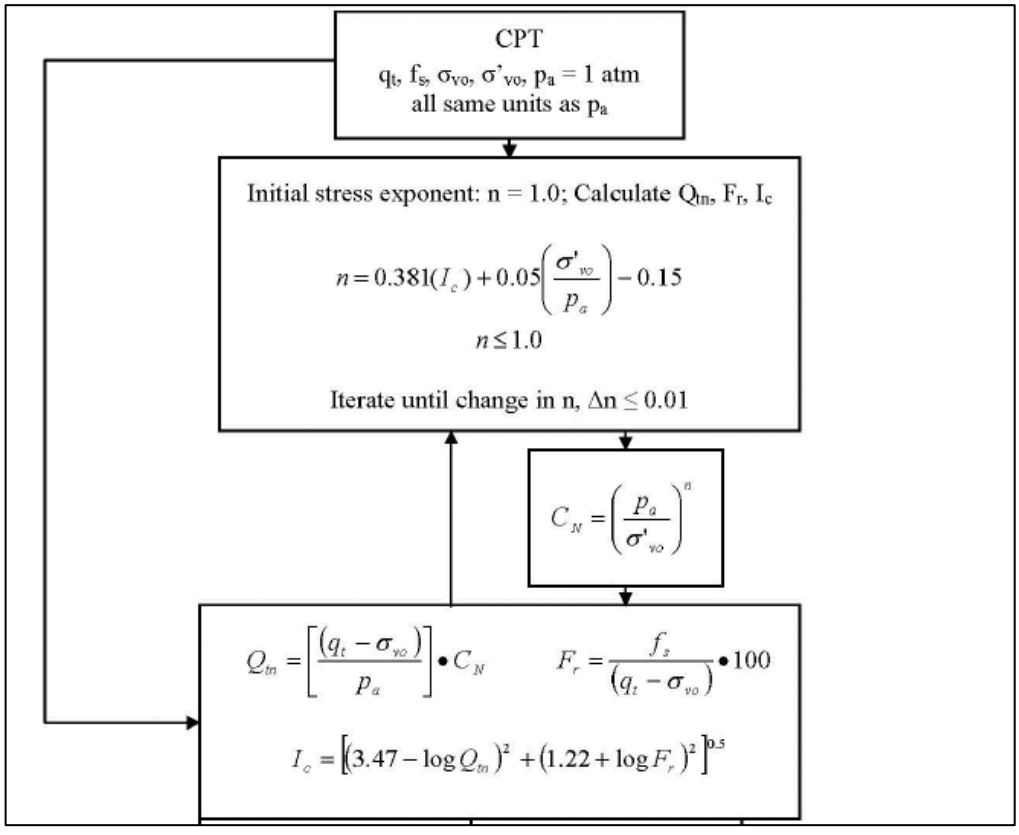

Figure B. 1: Iterative process for determining Ic from CPT (after Robertson, 2009)

1.2 Equivalent clean sand cone penetration resistance $(Q_{tn})_{cs}$

For a better identification of the soil layers, in addition to the Ic profiles, the equivalent clean sand cone penetration resistance $(Q_{tn})_{cs}$ profiles are determined.

Robertson and Cabal (2015) provide Equation (1.2) for calculating $(Q_{tn})_{cs}$

$$(Q_{tn})_{cs} = K_c Q_{tn} \tag{1.2}$$

where K_c is a correction factor function of behavior characteristics of soil calculated as:

$$K_c = 1.0 \text{, if } Ic \le 1.64$$

$$K_c = 5.581\,Ic^3 - 0.403\,Ic^4 - 21.63\,Ic^2 + 33.75\,Ic - 17.88 \text{, if } I_c > 1.64$$

A comparison between the Ic and corrected CPT profiles obtained from Green et al. (2008a) and Robertson and Cabal (2015) procedures is provided in Figure B. 2 for CPT 022. The Ic profiles are almost identical and the corrected CPT profiles are very comparable except for the upper 1 meter of the profile where the values calculated from Robertson and Cabal (2015) are higher than those obtained from Green et al. (2008a). However, the layers identified from both profiles are the same.

1.3 Equivalent SPT N_{60}

In the absence of SPT test results, CPT/SPT correlations are used to estimate the N_{60} values from CPT tests. Jefferies and Davies (1993) suggested a correlation between Ic and CPT/SPT ratios which was later improved by Robertson (2012). Equation (1.3) provides the Robertson (2012) correlation used to calculate N_{60} values:

$$\left(\frac{q_t / P_a}{N_{60}}\right) = 10^{(1.1268 - 0.2817 I_c)} \tag{1.3}$$

The N_{60} values obtained using Robertson (2012) correlation are corrected for overburden stresses using Peck et al. (1974) correlation:

$$N_{1,60} = N_{60} \times 0.77 \log\left(\frac{20}{\sigma_v'}\right) \text{ where } \sigma_v' \text{ is given in tsf or kg/cm}^2$$

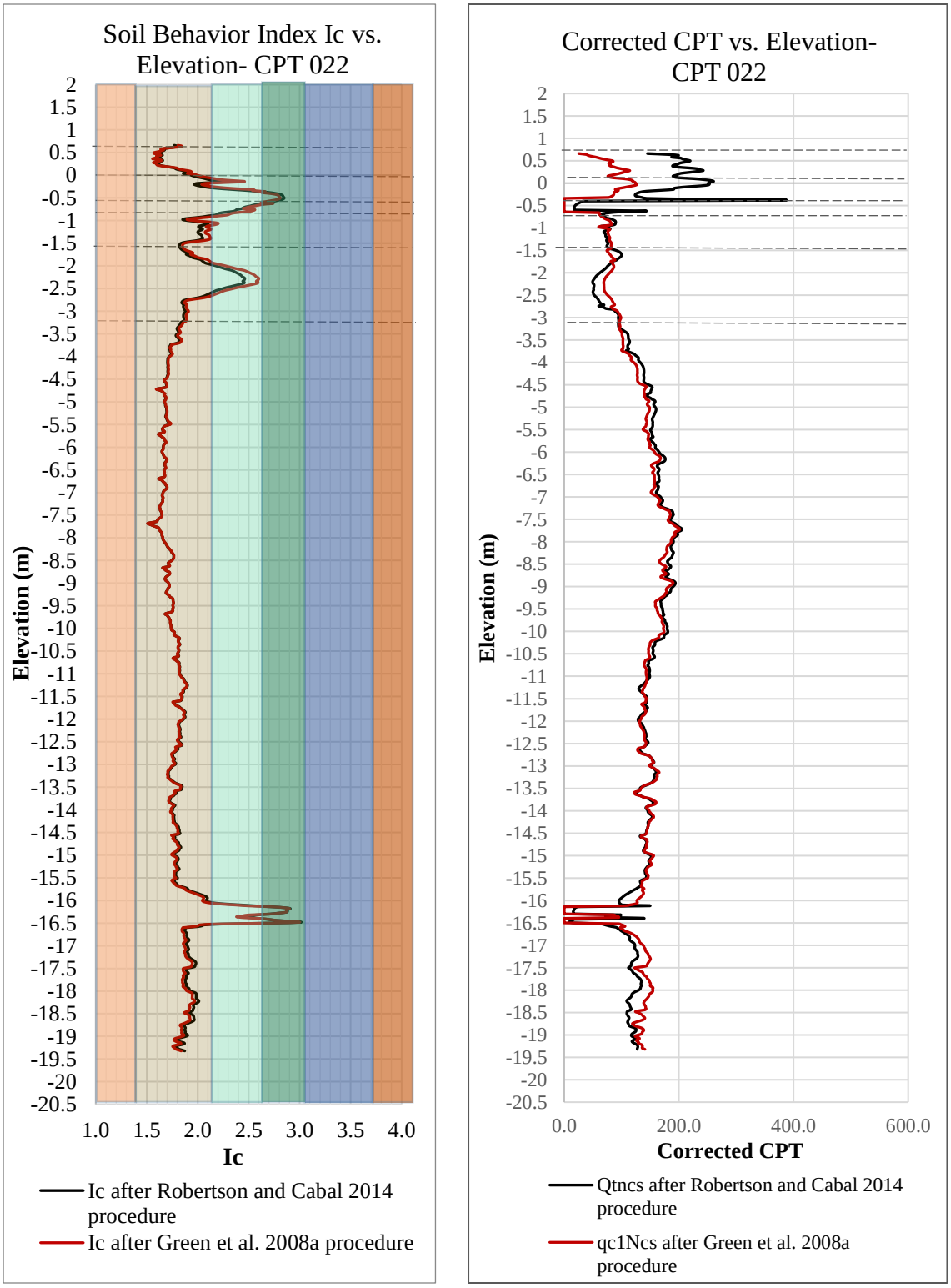

Figure B. 2: Comparison between Ic and corrected CPT profiles for Green et al. (2008a) and Robertson and Cabal (2015) procedures

1.4 Unit weight γ

The unit weight γ is estimated from the CPT data using Equation(1.4):

$$\gamma / \gamma_w = 0.27[\log R_f] + 0.36[\log(q_t / P_a)] + 1.236 \quad (1.4)$$

where:

R_f = friction ratio

$= (f_s / q_t) \times 100\%$

γ_w = unit weight of water (same units as γ)

1.5 Relative Density Dr

Numerous correlations between CPT resistance and relative density have been developed. The following three correlations were selected to have a general estimation of the relative density of the soils at Site 6 in Christchurch: Baldi et al. (1986), the simplified Kulhawy and Mayre (1990) and Jamiolkowski et al. (2001)

- The correlation provided by Baldi et al. (1986) is given in Equation (1.5):

$$Dr = \left(\frac{1}{C_2}\right) \ln\left(\frac{Q_{cn}}{C_0}\right) \quad (1.5)$$

where:

Q_{cn} = normalized CPT resistance, corrected for overburden

$= (q_c / P_a) / (\sigma'_{vo} / P_a)^{0.5}$

C_o and C_2 soil constants equal to 15.7 and 2.41 respectively for moderately compressible, normally consolidated, unaged and uncemented, predominantly quartz sands.

- The simplified Kulhawy and Mayne (1990) correlation for medium, uncemented, unaged quartz sand is provided in Equation (1.6):

$$Dr^2 = Q_{tn} / 350 \quad (1.6)$$

- Jamiolkowski et al. (2001) proposed Equation (1.7) for estimating relative densities of sand:

$$Dr = 100 \,.\, [0.268 \,.\, \ln(q_{t1}) - b_x] \tag{1.7}$$

where:

$$q_{t1} = \frac{(q_t / P_a)}{(\sigma'_{v0} / P_a)^{0.5}}$$

$$b_x = 0.675$$

1.6 Friction angle ϕ

Robertson and Campanella (1983) and Kulhawy and Mayne (1990) correlations are used to estimate the friction angle of the soil.

- Robertson and Campanella (1983) correlation given by Equation (1.8) estimates the friction angle from CPT for uncemented, unaged, moderately compressible, predominately quartz sands:

$$\tan\phi' = \frac{1}{2.68}\left[\log\left(\frac{q_c}{\sigma'_{v0}}\right) + 0.29\right] \tag{1.8}$$

- Equation (1.9) is provided by Kulhawy and Mayne (1990) for rounded quartz sands:

$$\phi' = 17.6 + 11\log(Q_{tn}) \tag{1.9}$$

1.7 Hydraulic conductivity k

The hydraulic conductivity (in m/s) can be estimated based on the normalized soil behavior index Ic using Equations (1.10) and (1.11):

$$k = 10^{(0.952 - 3.04Ic)}, \text{ for } 1.0 < Ic \le 3.27, \tag{1.10}$$

$$k = 10^{(-4.52 - 1.37Ic)}, \text{ for } 3.27 < Ic < 4.0. \tag{1.11}$$

The above equations should only be used as a guide for rough approximations of soil permeability.

2. Estimation of elastic soil properties from DPCH

The G value of each layer can be estimated from the soil densities (ρ) and V_s values using Equation (1.12), and the Young's Modulus can be estimated based on G values and Poisson's ratio using Equation (1.13) (Kramer,1996).

$$G = V_s^2 \times \rho \tag{1.12}$$

$$E = 2 \times G \times (1 + \nu) \tag{1.13}$$

The Poisson's ratio can be roughly estimated from the ratio of s-wave velocity to p-wave velocity (Kramer, 1996) as given in Equation (1.14)

$$\nu = \frac{1 - 2(V_s / V_p)^2}{2\left[(1 - V_s / V_p)^2\right]} \tag{1.14}$$

Appendix C: Calibration of Material Properties for Unreinforced FD Model

Five control points are defined in the FD model as given in Figure C. 1

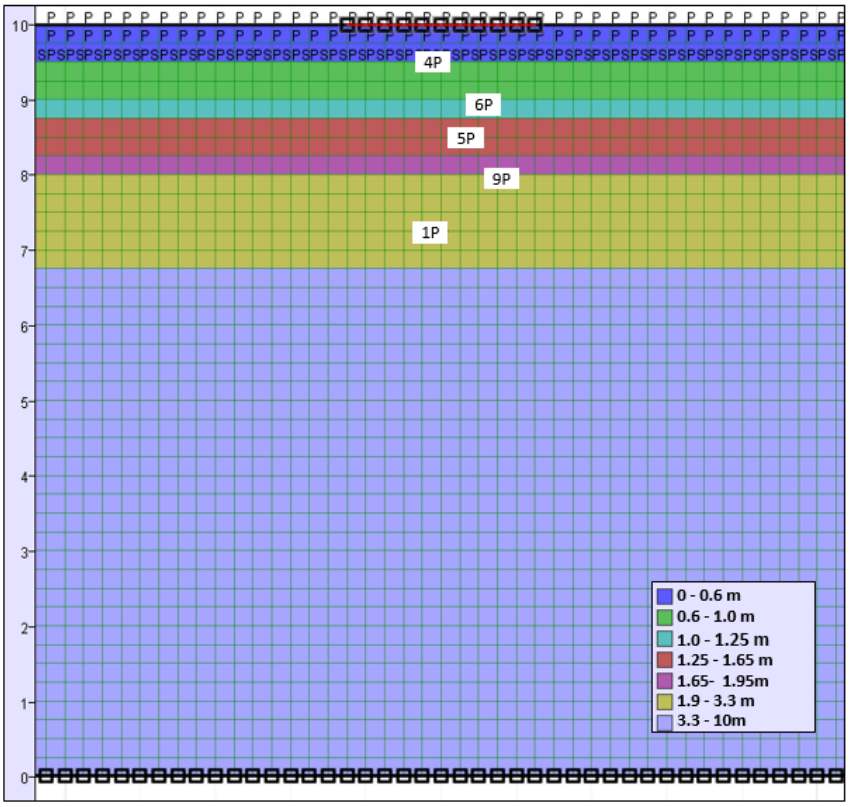

Figure C. 1: Control points defined in the FD model

1. Parametric study for the hydraulic conductivity parameter

Three different cases (Table C. 1) are considered in order to assess the extent to which the hydraulic conductivity values affect the results. In case 1, a distinction between the permeability of sand and that of the silty upper layers is made. In case 2, each layer is assigned an average value of hydraulic conductivity obtained from CPT 022 and CPT 065 (Table 3 and Table 4). Case 3 consists on refining the values adopted in case 2. The three different cases of this parametric study are conducted for a shear stress of 25 kPa.

For the five control points (Figure C. 1), the results corresponding to each case are provided in Figure C. 2, Figure C. 3, Figure C. 4, Figure C. 5 and Figure C. 6 using the same color

scheme as in Table C. 1 (case 1 in blue, case 2 in red, case 3 in brown). The different permeability cases do not introduce dramatic changes in the r_u values. However, case 3 seems to produce more stable results where numerical instabilities are avoided.

Table C. 1: Cases for hydraulic conductivity parametric study

	Case 1	Case 2	Case 3
Depth (m)	**Hydraulic conductivity (m/s)**	**Hydraulic conductivity (m/s)**	**Hydraulic conductivity (m/s)**
0 - 0.6	5E-08	9E-05	9E-05
0.6 -1	5E-08	7E-06	6E-07
1 - 1.25	5E-08	6E-07	6E-07
1.25 - 1.65	5E-08	1E-06	2E-05
1.65 - 1.9	5E-08	2E-05	2E-05
1.9 - 3.3	5E-05	2E-05	2E-05
3.3 - 10	5E-05	7E-05	7E-05

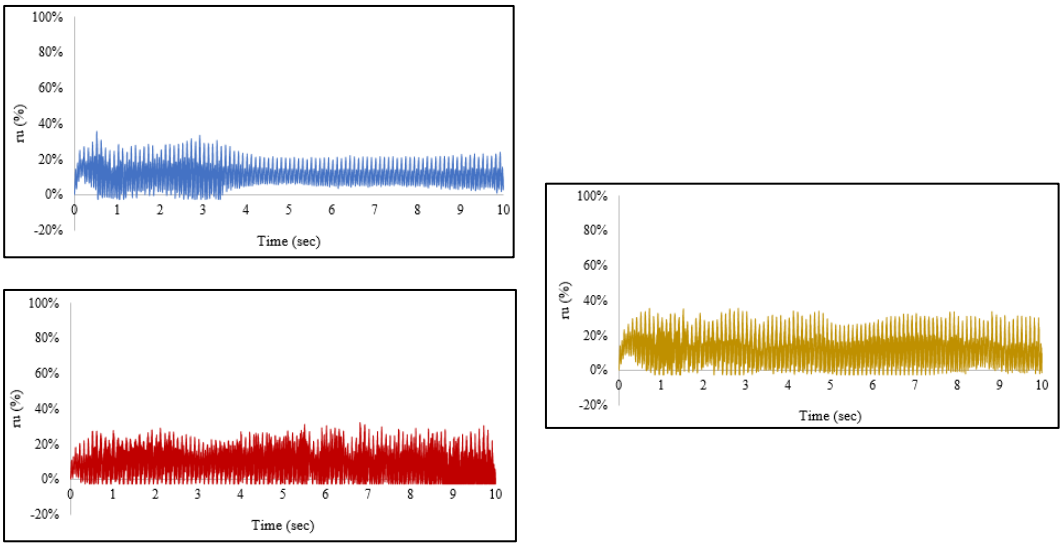

Figure C. 2: Evolution of r_u at control point 4P for different hydraulic conductivities

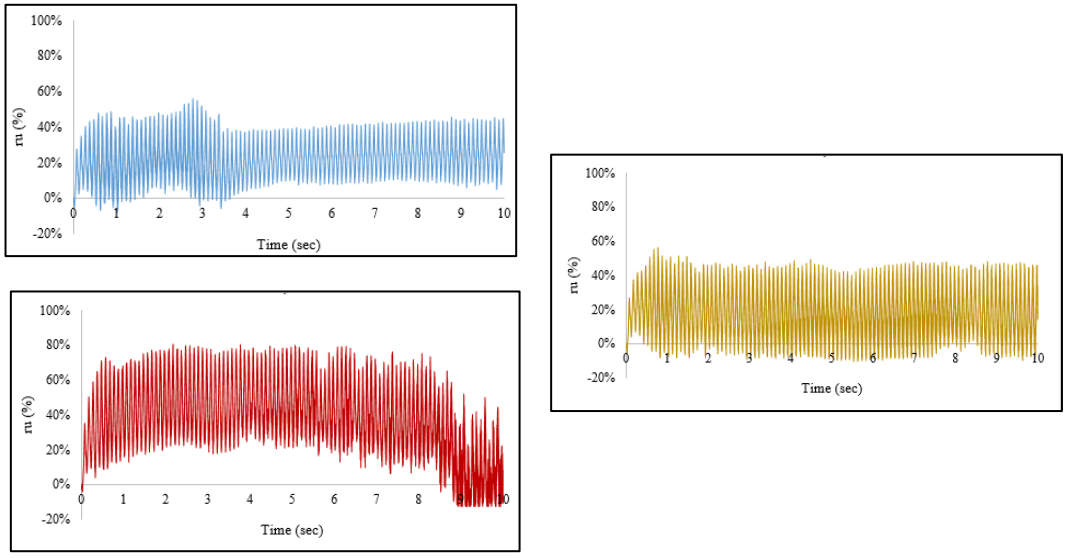

Figure C. 3: Evolution of r_u at control point 6P for different hydraulic conductivities

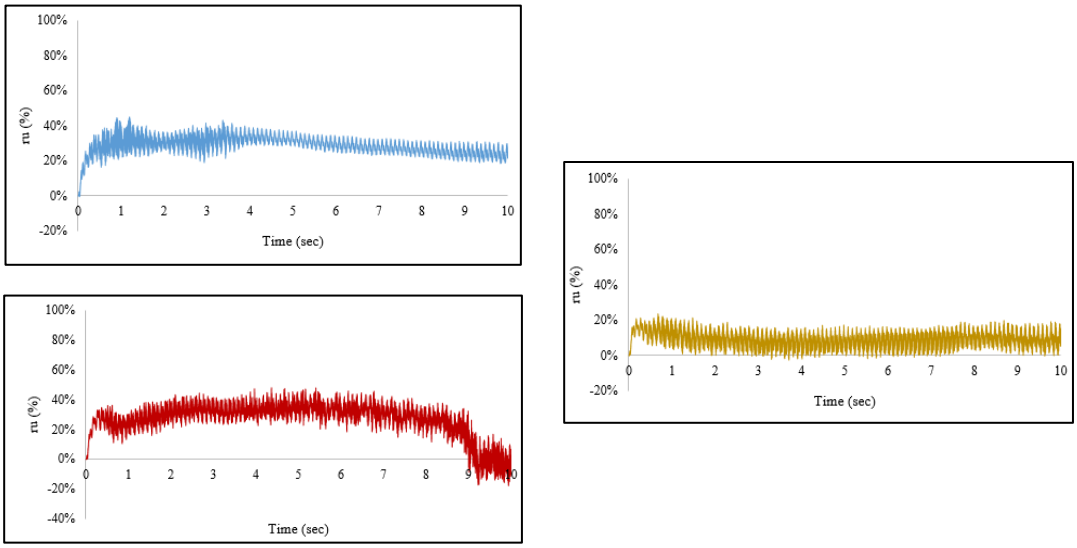

Figure C. 4: Evolution of r_u at control point 5P for different hydraulic conductivities

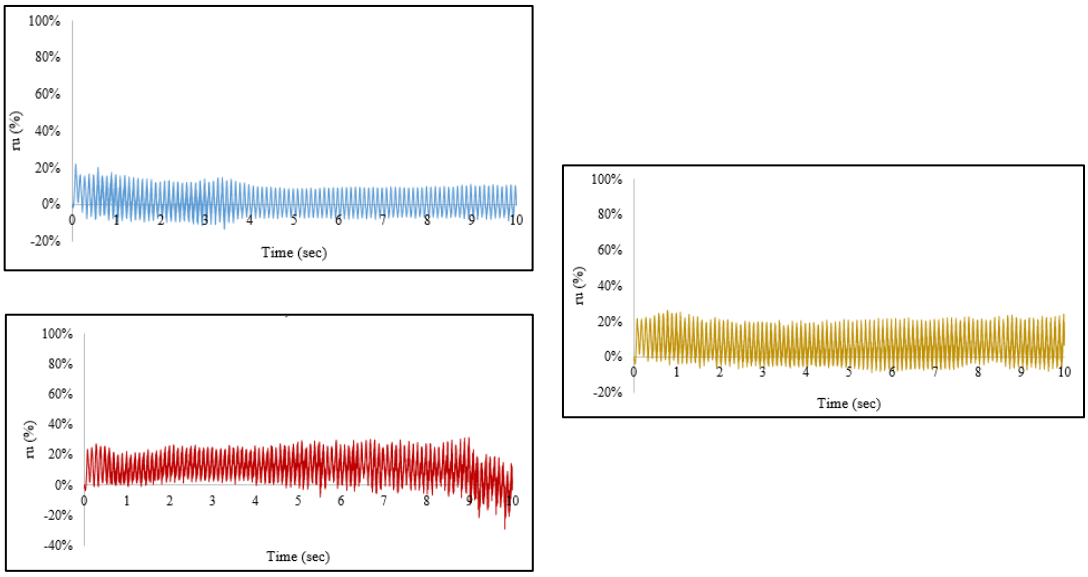

Figure C. 5: Evolution of r_u at control point 9P for different hydraulic conductivities

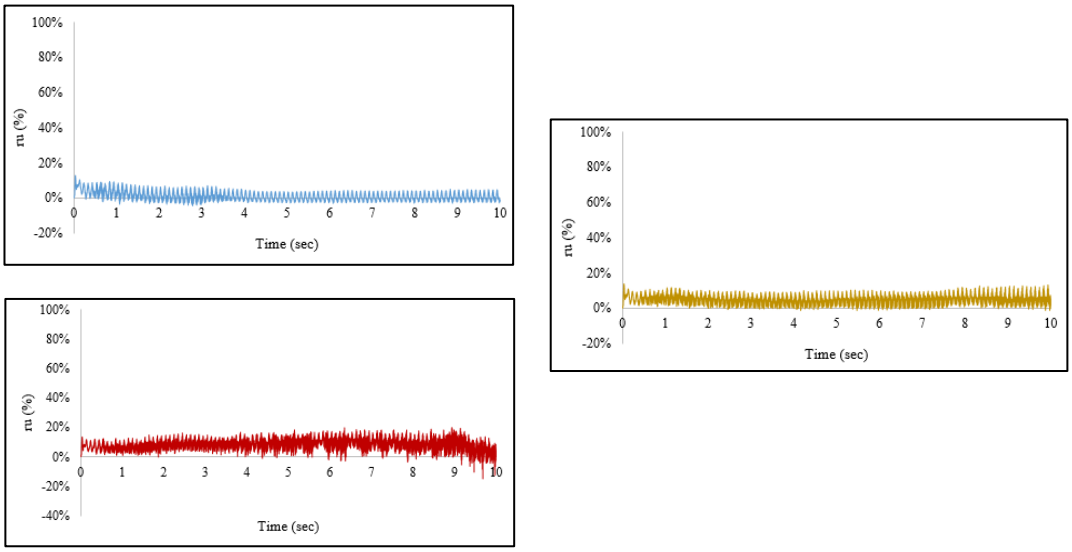

Figure C. 6: Evolution of r_u at control point 1P for different hydraulic conductivities

2. Parametric study for the shear modulus

As explained in section 2.8.8, three cases of shear modulus are considered: lower range of G from DPCH 35261, higher range of G from DPCH 35269 and average values of G. The results obtained for a cyclic shear stress of 15 kPa and a Poisson's ratio of 0.45 are provided in Figure C. 7 and they are compared to the unimproved in-situ profile (6-NS-2).

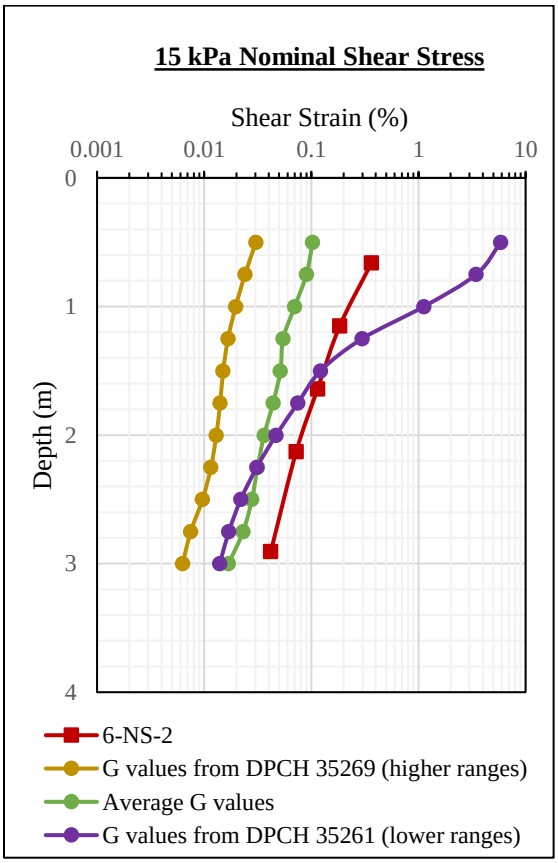

Figure C. 7: Shear modulus calibration for a Poisson's ratio = 0.45 and cyclic shear stress of 15 kPa

Three cases of Poisson's ratio values are then considered: 0.48, 0.45, and 0.40 and the results are shown in Figure C. 8.

The case of average G values is adopted and the shear strain profiles obtained for 5, 15 and 25 kPa for different Poisson's ratio values are provided in Figure C. 9. The in-situ strain profile is not available for a load of 25 kPa and is therefore missing from Figure C. 9.

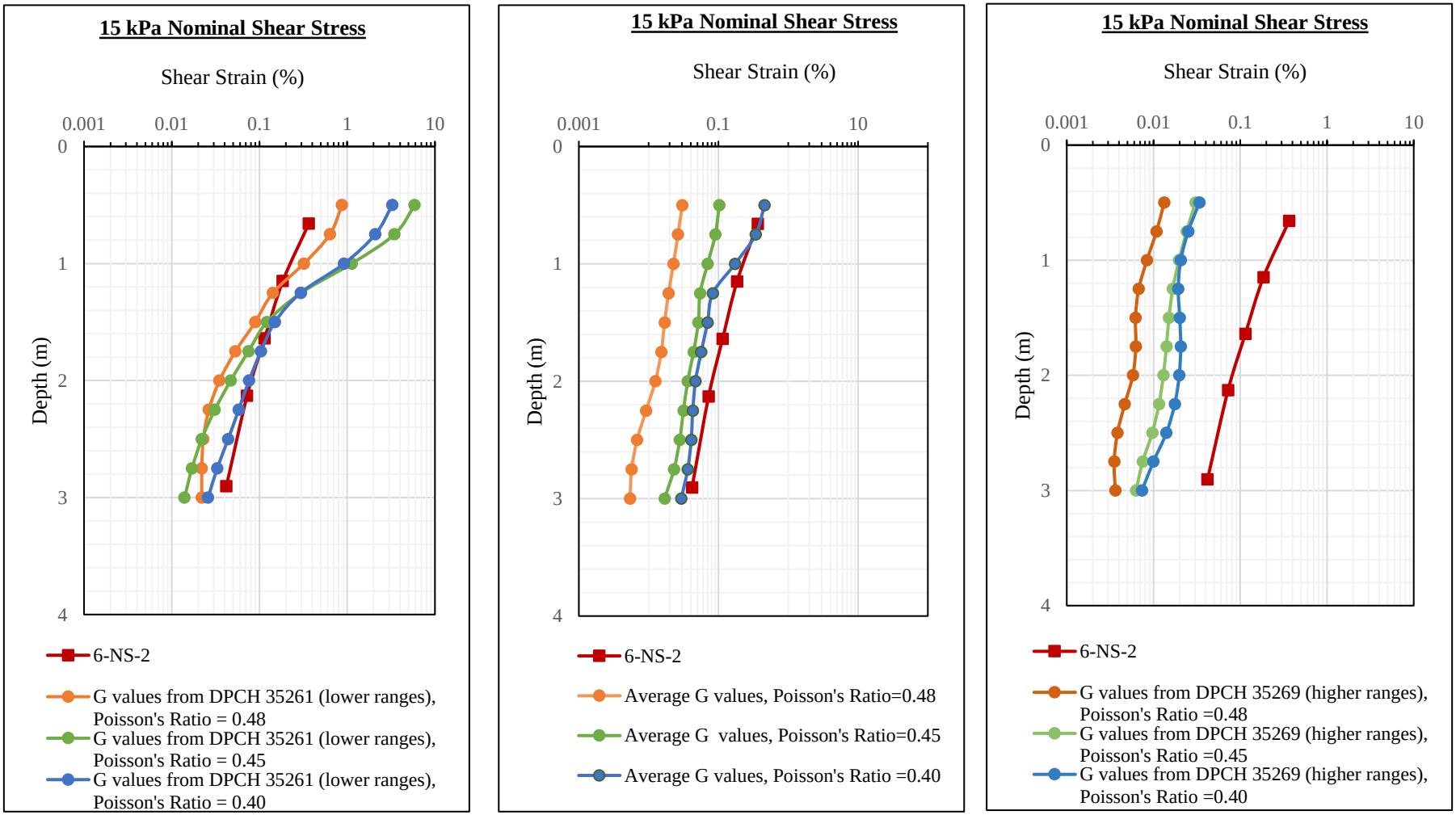

Figure C. 8: Poisson's ratio calibration for a cyclic shear stress of 15 kPa, using G values from DPCH 35261 (left), DPCH 35269 (right), and averaged values (middle)

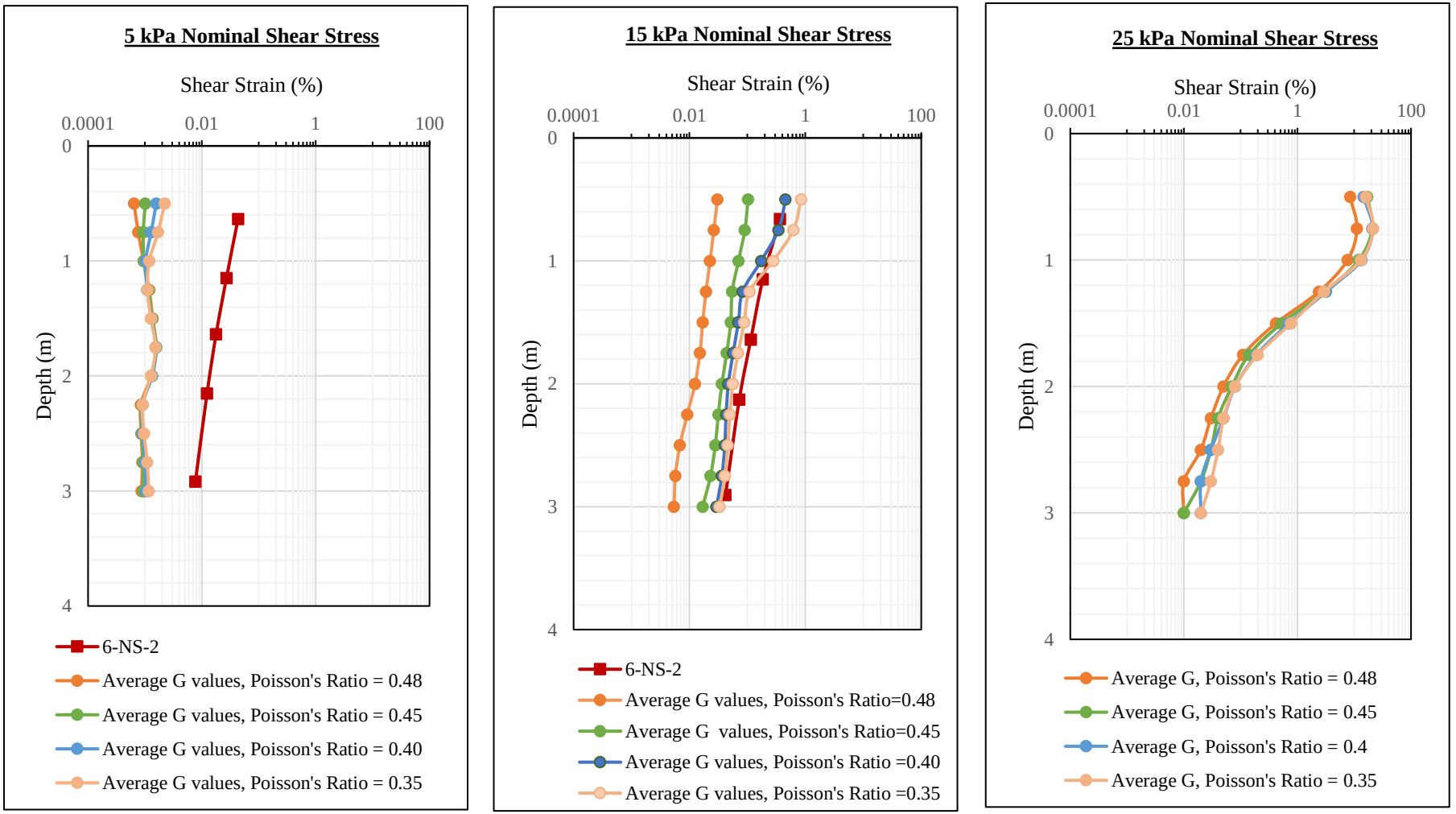

Figure C. 9: Poisson's Ratio calibration for average G values and cyclic shear stresses of 5, 15 and 25 kPa, using average G values from DPCH 35261 and DPCH 35269.

Appendix D: Vertical Stress, Pore Pressure, and Volumetric Strain Distributions for the Unreinforced FD Model

1. Numerical results after the gravity loading (Stage 1)

The total and effective vertical stress, and pore pressure distributions after the application of the gravity loading are provided in Figure D. 1, Figure D. 2, and Figure D. 3 respectively. Note that a description of the sign conventions in FLAC v.8 relevant to the output results is provided in Appendix F.

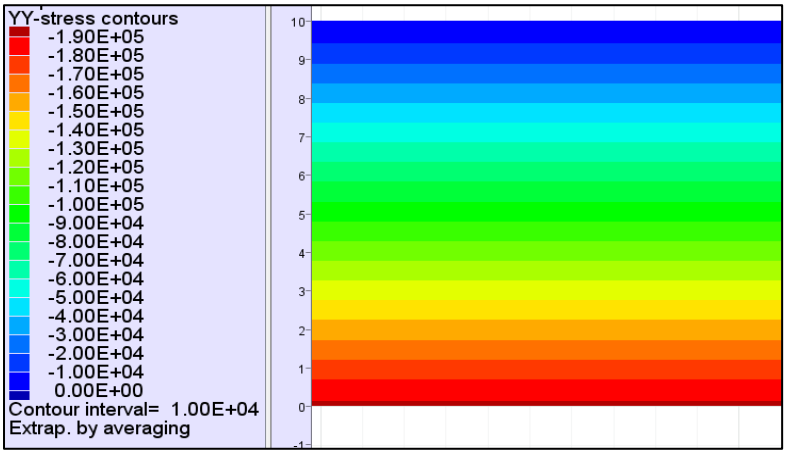

Figure D. 1: Total vertical stress distribution after gravity loading

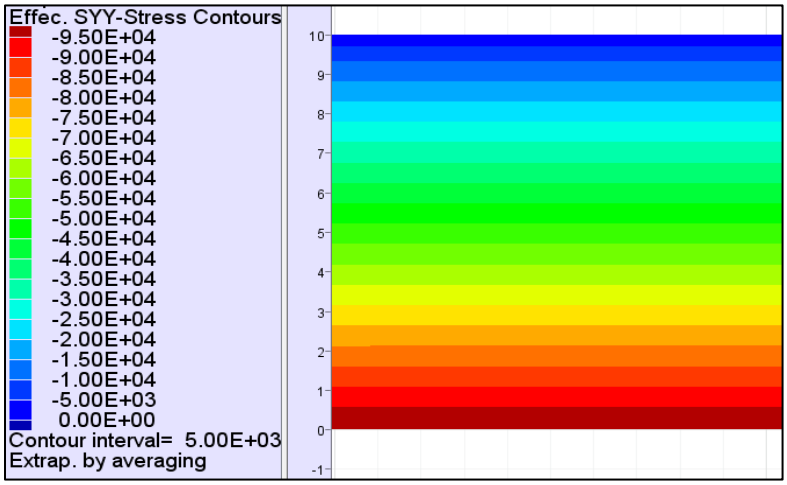

Figure D. 2: Effective vertical stress distribution after gravity loading

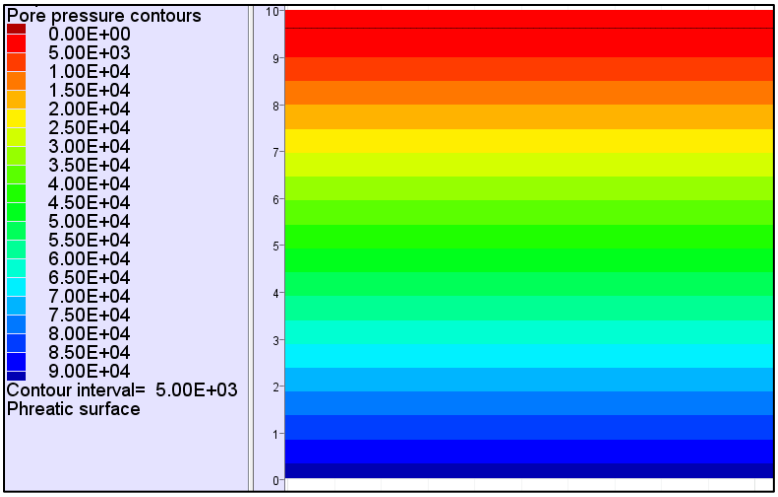

Figure D. 3: Pore pressure distribution after gravity loading

2. Numerical results after the application of vertical loading (Stage 2)

The total and effective vertical stress, pore pressure, and volumetric strain distributions after the application of the vertical loading (46 kPa) are provided in Figure D. 4, Figure D. 5, Figure D. 6, and Figure D. 7 respectively. Vertical stresses increase as a result of the vertical loading. The pore water pressure distribution presents a hydrostatic profile and is identical to the one presented in Figure D. 3 since the excess of pore water pressure generated by the external load is fully dissipated. Negative volumetric strains decreasing with depth are generated under the baseplate as a result of the consolidation process.

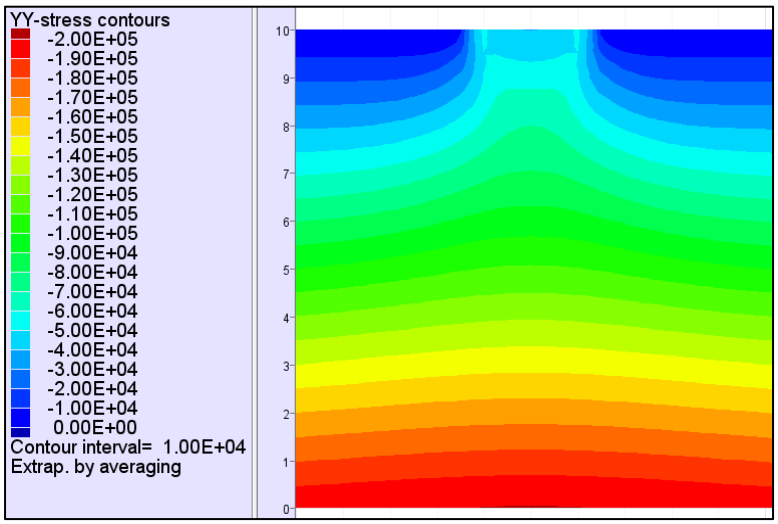

Figure D. 4: Total Vertical stress distribution after the application of vertical loading

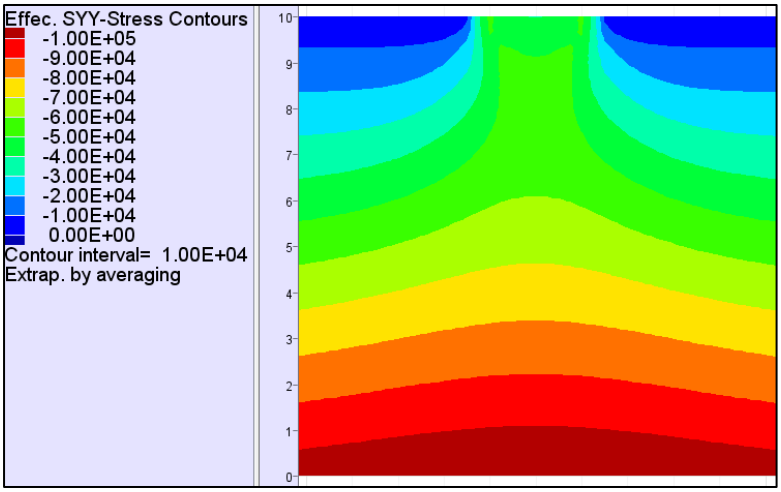

Figure D. 5: Effective vertical stress distribution after the application of vertical loading

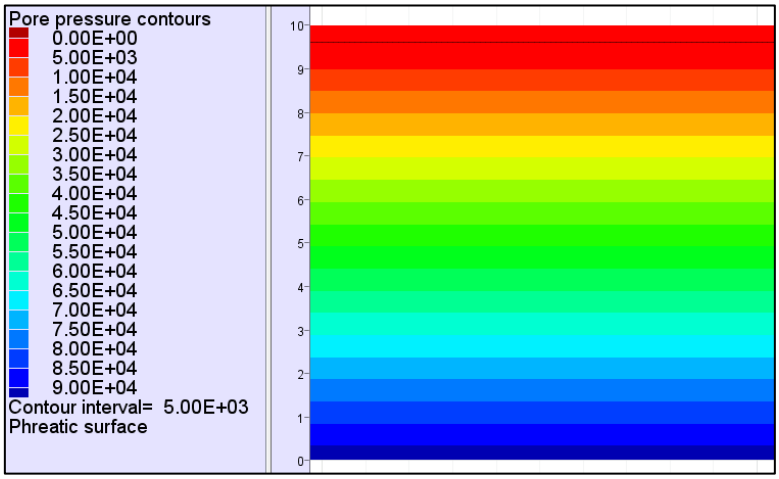

Figure D. 6: Pore pressure distribution after the application of vertical loading

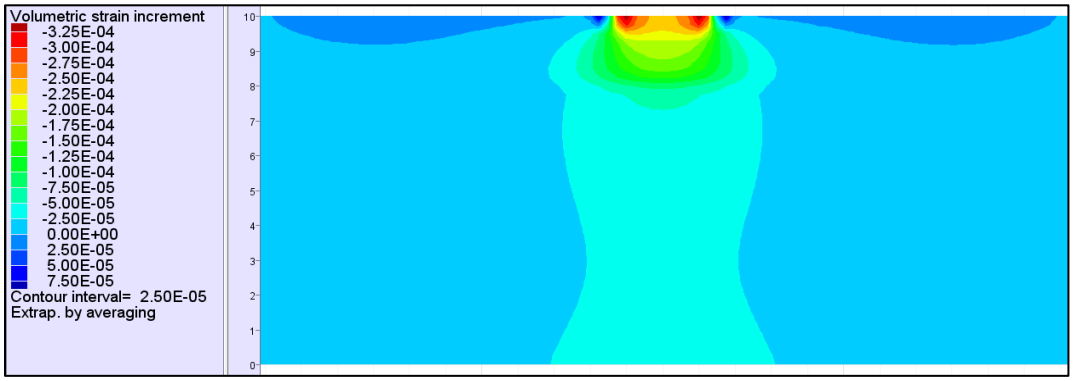

Figure D. 7: Volumetric strain distribution after the application of vertical loading

3. Numerical results after the application of the cyclic shear load (Stage 3)

The total and effective vertical stress and pore pressure after the application of the cyclic horizontal loading are provided in Figure D. 8, Figure D. 9, and Figure D. 10 respectively, for cyclic shear stresses of 25 kPa and 2.5 kPa. Generation of pore pressure takes place especially under the baseplate causing a decrease in the effective stresses in this area.

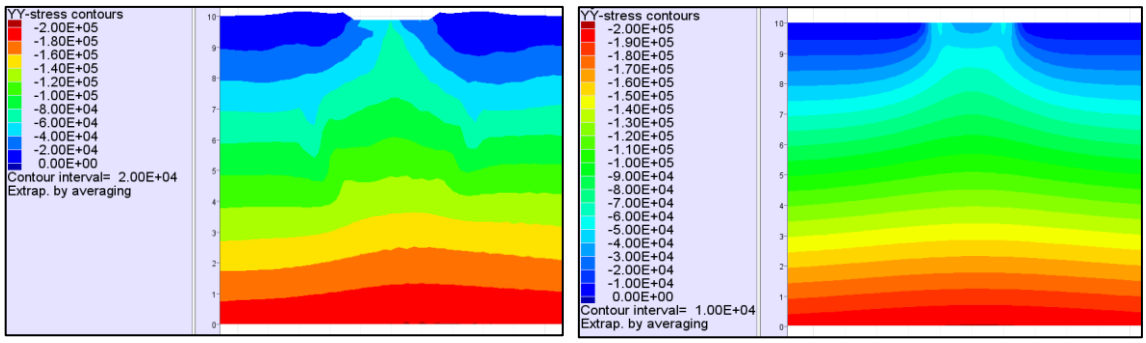

(a) **(b)**

Figure D. 8: Total vertical stress distribution after a cyclic shear stress of (a) 25 kPa; and (b) 2.5 kPa

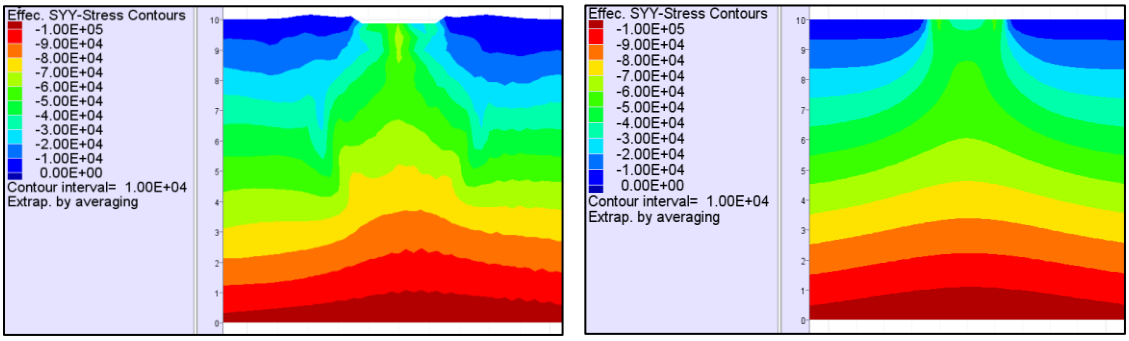

(a) **(b)**

Figure D. 9: Effective vertical stress distribution after a cyclic shear stress of (a) 25 kPa; and (b) 2.5 kPa

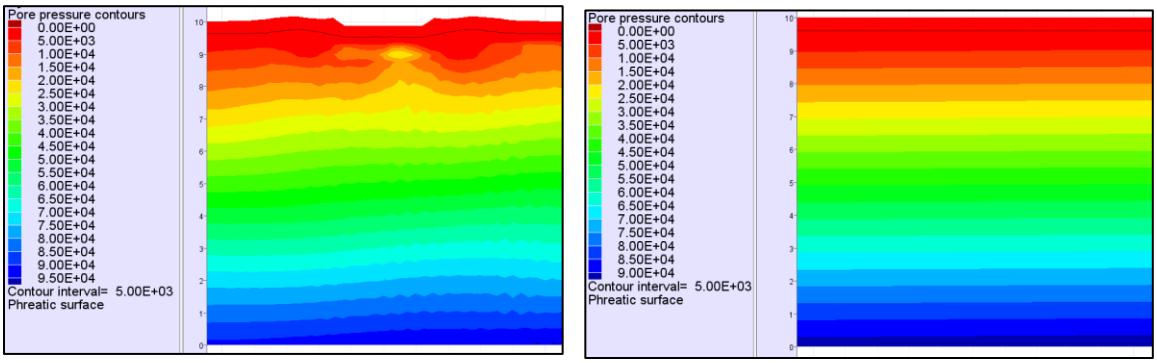

(a) **(b)**

Figure D. 10: Pore pressure distribution after a cyclic shear stress of (a) 25 kPa; and (b) 2.5 kPa

Appendix E: Shear Velocity Profile for Deconvolution Analysis

The shear velocity profile is estimated using the Christchurch specific CPT-V_s correlation provided by McGann et al. (2014):

$$V_s = 18.4 q_c^{0.144} f_s^{0.0832} z^{0.278}$$

CPT-Bex-14 with a maximum depth of 39.2 m is the deepest CPT sounding available in the vicinity of Site 6. q_c and f_s are therefore obtained from CPT-Bex-14 and V_s are calculated and plotted against the elevation. The V_s profile as well as the digitized profile used in Strata for the deconvolution analysis are provided in Figure E. 1. The maximum V_s value estimated at an elevation of 38 m is around 332 m/s.

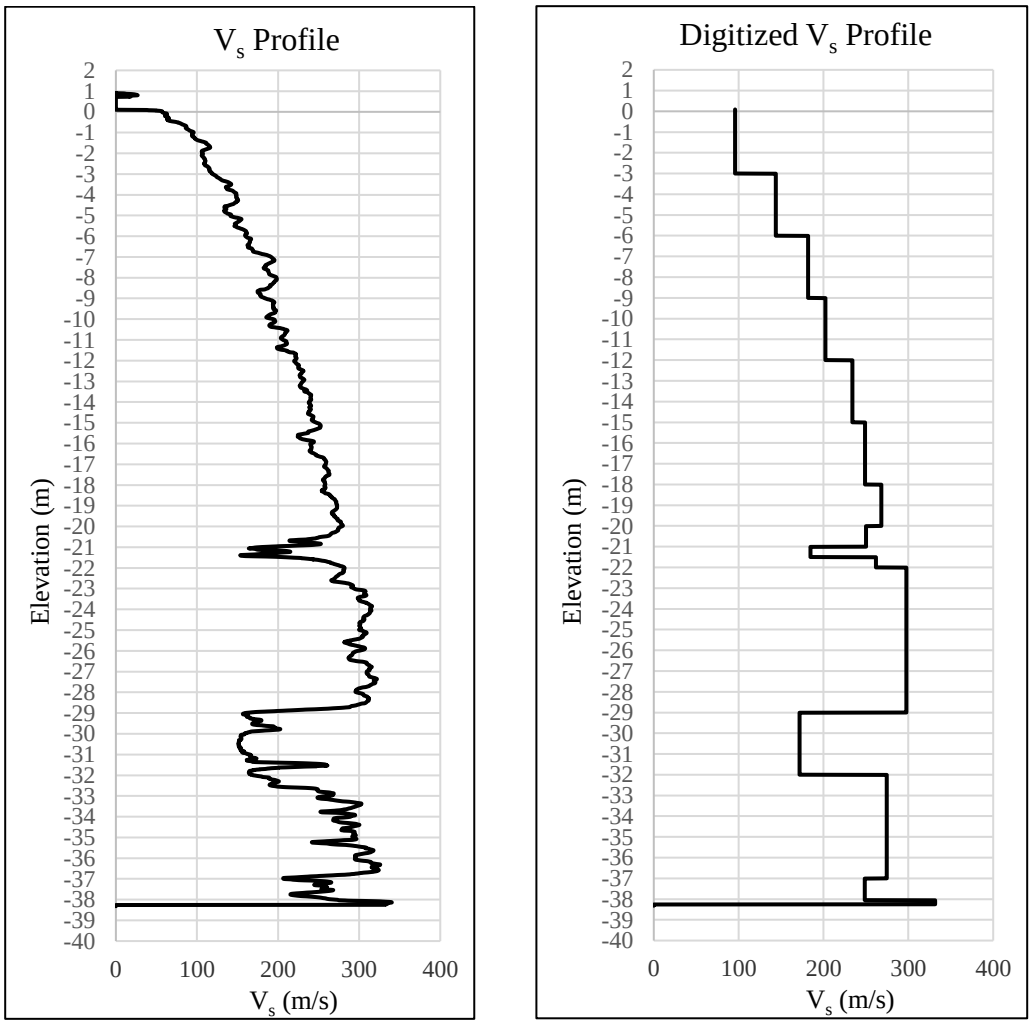

Figure E. 1: Vs profile estimated for the deconvolution analysis

Appendix F: Sign Conventions and System of Units in FLAC v.8

A description of the sign conventions in FLAC v.8 relevant to the output results is provided in Table F. 1 and Figure F. 1.

Table F. 1: Sign conventions for direct stress and strain and pore pressure in FLAC v.8

Parameter	Positive Sign	Negative Sign
Direct Stress	Tension	Compression
Direct Strain	Extension	Compression
Pore pressure	Compression	Tension

Sign conventions for shear strains follow the convention of shear stresses, which are positive when they act as shown in Figure F. 1. The distortion associated with shear strains are also presented in Figure F. 1.

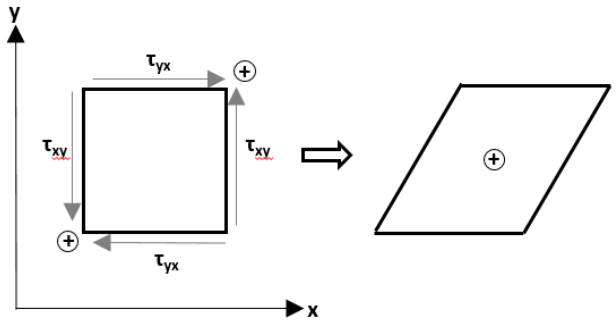

Figure F. 1: Sign convention for positive shear stress and distortion associated with positive shear strain (After FLAC Manual v.8).

Table F. 2 summarizes the set of system units for input and output parameters in the FLAC analysis.

Table F. 2: System units in the FLAC analysis

Parameter	Unit
Length	m
Density	kg/m^3
Stress	Pa
Gravity	m/sec^2
Water Bulk Modulus	Pa